Level 2 Photometric Calibration for the LSST Survey

R. Lynne Jones[1], Željko Ivezić[1], Tim Axelrod[2], David Burke[3],
James G. Bartlett[4], Gurvan Bazin[4], Guillaume Blanc[4], Michel Crézé[4],
Cécile Roucelle[4], Abhijit Saha[5], J. Allyn Smith[7] Michael A. Strauss[6]
on behalf of The Photometric Calibration Team
Docushare-8123, –/–/–

ABSTRACT

This document describes the photometric calibration procedure for LSST Data Release catalogs. This procedure will use specialized hardware, an auxiliary telescope, an atmospheric water vapor measurement system, and narrowband dome screen illuminator, to measure the wavelength dependence of the atmospheric and hardware response functions, together with a self-calibration procedure that leverages multiple observations of the same sources over many epochs, to deliver 1%-level photometry across the observed sky.

Contents

[1]University of Washington

[2]University of Arizona

[3]SLAC National Accelerator Laboratory

[4]APC, Universite Paris Diderot

[5]NOAO

[6]Princeton University

[7]Austin Peay State University

1. Introduction

LSST is required to deliver 1%-level photometry across the observed sky and under a wide range of observing conditions (0.5%-level for repeat observations of the same source). This represents about a factor of two improvement over the current state-of-the-art wide-field optical photometry delivered by SDSS under photometric conditions. This factor of two improvement will have a major impact on science deliverables because it implies that the error volume in the five-dimensional LSST color space will be over thirty times smaller than for SDSS-like photometry. This smaller error volume will improve source classification and the precision of quantities such as photometric redshifts for galaxies and photometric metallicity for stars. For example, a given spectral energy distribution (SED) corresponding to some galaxy type produces a line in the *ugrizy* multi-dimensional color space when redshifted, where the position of the galaxy along that line in *ugrizy* space is a function of redshift. Different galaxy SEDs produce lines that are often close to each other in *ugrizy* space and sometimes even cross. The smaller the error volume around an observed galaxy's measured *ugrizy* colors, the smaller the number of different lines (thus, different SEDs) and different positions along the line (thus, different redshifts) which will be consistent with the measurement. The same conclusion is valid in the case of algorithms that estimate stellar effective temperature and metallicity, as well as any other model-based interpretation of measurements. Furthermore, the smaller error volume per source is advantageous even in the absence of any models. Two sources whose color differences produce a value of χ^2 per degree of freedom of 1, will have a χ^2 per degree of freedom of 4 when the errors are halved. In case of five degrees of freedom, χ^2 pdf > 4 will happen by chance in only 0.1% of all cases. Therefore, the ability to reliably detect color differences between sources is a strong function of photometric errors.

The factor of two reduction in photometric error results from two major differences

between LSST and SDSS. First, each source will receive hundreds of observations over the ten years of the LSST survey. These series of repeat observations will be used to self-calibrate the photometric system across the sky and for each observation (akin, but not identical to, the uber-calibration procedure used by SDSS (**?**)), allowing LSST to operate in a wide variety of conditions. Secondly, the wavelength dependence of the hardware and atmospheric transmission response functions will be measured with auxiliary instrumentation on sufficiently fine angular and temporal scales to enable their explicit inclusion in the calibration procedure, rather than resorting to traditional approximations such as linear color terms. SNLS re-processing of CFHT Legacy Survey data found these color-dependent terms to be a significant contributor to the photometric calibration process (**?**), on the level of a few to several percent. **TODO here on why it's hard - drift scan and all weather**

This document describes the calibration requirements and processes for LSST Data Release photometry. At each Data Release, there will be a complete recalibration of all data acquired to that point, on approximately an annual schedule. These data products are referred to as Level 2 Data Products. There will also be a real-time data calibration process, based on the best available set of prior calibrated observations, to provide real-time, but lower quality, photometry for quality assurance, generation of alerts, and other quantities appropriate for nightly data generation (aka Level 1 Data Products). The Level 1 photometric calibration is not discussed here.

Section 2 reviews the survey requirements for photometric calibration, while Section 3 describes the foundation of LSST's calibration procedure, first motivating this procedure by describing the true path of a photon through the atmosphere and LSST system and then from the calibration point of view, trying to recreate the transmission of those photons to the focal plane. Section 5 describes details of each step of the calibration procedure, including how each calibration measurement is obtained and applied to the science data along with expected errors originating from each step. Section 4 describes how the LSST's internal photometric scale is tied to external references. Section 7 describes how we will verify that the calibration system functions as designed, and meets the science requirements, first during the construction phase, and later during survey operations.

2. Photometric Requirements

The LSST Science Requirements Document (SRD) provides a set of requirements on the annual Data Release (Level 2) photometry. These requirements are extended in the XXX (OSS) to cover aspects which are too detailed for the SRD. based on measurements of bright, unresolved, isolated, non-variable objects from individual LSST visits. **TODO**

- address what these requirements actually apply to. MS stars vs other SEDs and reference App C. Also be explicit that calibration is based on objects with well-known SEDs - i.e. MS stars. Bright implies that the measurement of the star's brightness is not dominated by photon statistics, approximately 1-4 magnitudes fainter than the saturation limit in a given filter. Isolated implies that the star can be successfully deblended from background galaxies and other stars. Non-variable objects are intrinsically not variable; these will be identified in an iterative fashion from the many epochs of LSST observations. The SRD specifications are:

1. **Repeatability:** the median value of the photometric scatter for each star (the rms of calibrated magnitude measurements around the mean calibrated magnitude) shall not exceed 5 millimags in gri, 7.5 millimags in uzy for bright, unresolved, isolated, non-variable objects. No more than 10% of these objects should have a photometric scatter larger than 15 mmag in gri, 22.5 mmag in uzy. This specifies the distribution of photometric errors (σ) and constrains both the repeatability of extracting counts from images and the ability to monitor (or model) the changes in the system response. It could be thought of as requiring the photometry of a single source to be consistent over time.

2. **Uniformity:** the rms of the internal photometric zeropoint error (for each visit) shall not exceed 10 millimags in $grizy$, 20 millimags in uzy, where the zeropoint for each visit is determined using bright, unresolved, isolated, non-variable sources. No more than 10% of these sources should be more than 15 mmag in gri or 22.5 mmag in uzy from the mean internal zeropoint. This places a constraint on the stability of the photometric system across the sky as well as an upper limit on various systematic errors, such as any correlation of photometric calibration with varying stellar populations (or colors). This makes the photometry of many sources comparable over the entire sky, and when combined with the previous requirement, creates a stable photometric system across the sky and over time, in a single filter.

3. **Band-to-band photometric calibration:** The absolute band-to-band zeropoint calibration for main sequence stars must be known with an rms accuracy of 5 millimags for any color not involving u band, 10 millimags for colors constructed with u band photometry. This places an upper limit on the systematic error in the measurement of the system throughput as a function of wavelength. This requirement ties photometric measurements in different filters together, enabling precise measurement of colors.

4. **Absolute photometric calibration:** The LSST photometric system must transform to an external physical scale (*e.g.* AB mags) with an rms accuracy of 10 millimags.

This requirement not only ties LSST internal photometry to photometry obtained from other telescopes, using other photometric systems, but also ties LSST internal photometry to a real physical scale. This places a constraint on the upper limit of the systematic error in the measurement of the total system throughput. This final step enables LSST photometry to be compared directly to data from other telescopes or to models (*e.g.* such as determining the albedo of an asteroid with a known diameter).

Requirements 1 and 2 must be met by measuring and then correcting for changes in hardware and atmospheric transmission as a function of time, location in the sky or focal plane, and result in a relative calibration within a single filter. Requirements 3 and 4 require comparison of LSST measurements to externally calibrated spectrophotometric standards, providing a relative calibration from filter to filter as well as an absolute physical scale for the overall system. Performance of the LSST system regarding requirement 1 can be verified by simply measuring the rms of the calibrated magnitude measurements. Verification of requirement 2 is more complicated; in a simulated system it is simple to compare the (simulated, thus known) true magnitudes of the stars to the best-fit magnitudes produced after calibration. **TODO forward reference new section on verification - Tim to write** In operations, this will be verified using a combination of simulations, comparisons to known standards, and evaluation of science outputs such as stellar locus diagrams. These last two tests are also relevant to verifying the final two requirements, 3 and 4.

TODO - Lynne (or someone) to verify consistency with new SRD reqs, *after* updating rest of doc and seeing effect of including new SEDs in SRD requirements. Plus need update of SRD to verify.

3. The Photometric Calibration Process

In traditional photometric calibration, a set of standard stars are observed at a range of airmasses to calculate zeropoint offsets and (typically) a single color-dependent extinction curve per night. With care, this approach can deliver 1% photometry in stable photometric conditions. Such programs typically follow only a few objects, and devote roughly equal time to standards and program objects. This approach fails for a survey like LSST, for at least two reasons. First, from a calibration point of view, the very wide field and multiple detector array mean that multiple instruments must be calibrated rather than just one. Second, historical weather data from Cerro Pachón tells us only 53% of the available observing time can be considered photometric even at the 1–2% level. To take advantage of the full 85% of the available observing time which is usable (total cloud extinction less than 1.5 magnitudes), and to reach the SRD specified requirements – 0.5% level photometric repeatability and 1%

photometric uniformity – requires a new approach.

This new approach, variants of which have been used at PanSTARRS and DES, lies in splitting the measurement of the *normalization* of the throughput in each observation (the gray-scale zeropoint) from the *shape* of the throughput curve (the color dependent terms), and further, using separate procedures to measure the individual contributions of the telescope hardware response and the atmospheric throughput. This calibration system requires various pieces of hardware to conduct these optimized measurements. We briefly describe them here, with full descriptions in the sections indicated:

- A dome screen projector designed to provide uniform ($\sim 10\%$ variation) illumination across the field of view, while minimizing stray light. This projector system will have the capability to not only illuminate the screen with broadband white light, but also narrow-band light to measure the system response at individual wavelengths. The narrow-band light will be generated by a tunable laser, capable of producing light from $300 - 1100$ nm and tunable in 1 nm increments. The brightness of the screen is measured with NIST-calibrated photodiodes, so that the relative intensity at different wavelengths is precisely determined. See Sections **??** and **??** for more information.

- A 1.2-m auxiliary telescope with an $R \approx 400$ spectrograph, located adjacent to the LSST itself. This auxiliary telescope will obtain spectra of a chosen set of atmospheric probe stars across the sky to determine an atmospheric absorption model. More details are provided in Section **??**.

- Water vapor monitoring system, consisting of a GPS system and a microwave radiometer attached copointed with the LSST telescope, and monitoring the same field of view. This supplements the auxiliary telescope spectra, which are unable to track the sometimes rapid variations of water vapor in time and space.

An overview of the entire calibration process, from science observation to calibrated photometric measurements, together with the required calibration data products is shown in Figures 1, 2, 3, and 4. Note that four classes of objects participate in the calibration process in different ways:

- Standard stars. These are stars whose absolute flux as a function of wavelength above the atmosphere is precisely known. This class contains only a few members, perhaps as few as ten. Their role is to enable the self calibration process to set absolute zeropoints for each band, and to allow testing of the SRD uniformity requirements. See Section 4.

- Calibration stars. These are stars that densely cover the sky, with typical spacings between stars of 1 arcminute. [NOTE: check this number]. Unlike standard stars, neither their SEDs nor their absolute fluxes are precisely known, and their standard magnitudes are determined by the self calibration process. They have been selected to be on the stellar main sequence, to be nonvariable, and to be relatively isolated so that their photometry is not degraded by crowding effects.

- Atmospheric probe stars. These are bright stars of known type, distributed roughly uniformly over the LSST sky, which yield high SNR spectra from the auxiliary telescope. This is particularly critical for calibrating the y-band.

- Science objects. Calibration of science objects utilizes the results of processing the standards and the calibration stars, and the measurement of the system bandpass. If an SED is supplied for an object, an accurate standard magnitude can then be calculated.

The rest of this section will provide a more in-depth overview of the calibration process. We will start with a review of what is physically happening to photons in their path toward the focal plane, and then outline how LSST will translate the measured ADU counts back to fluxes above the atmosphere.

We find it helpful to define four different magnitudes, and their associated fluxes:

- m_b^{inst}, the instrumental magnitude. $m_b^{inst} = -2.5 log10(C_b^{obs})$, where C_b^{obs} are the instrumental counts (ADU) that are attributed to the object

- m_b^{nat}, the natural magnitude. This is the magnitude in the AB system that would be measured for the object if it were measured through the actual normalized system bandpass, $\phi_b^{obs}(\lambda)$, at the top of the atmosphere. This bandpass varies from exposure to exposure. See equations 7 and 9. $m_b^{nat} = m_b^{inst} + Z_b^{obs}$

- m_b^{std}, the standard magnitude. This is the magnitude in the AB system that would be measured for the object if it were measured through the standard normalized system bandpass, $\phi_b^{std}(\lambda)$, at the top of the atmosphere. This bandpass is selected as part of the survey design, and does not vary. See equation 8.

- m_b^{corr}, the SED corrected instrumental magnitude. This is the standard magnitude, but with an unknown gray zeropoint correction, which will be removed by self calibration. These magnitudes are the input to self calibration. $m_b^{corr} = m_b^{inst} + \Delta m_b^{obs}$

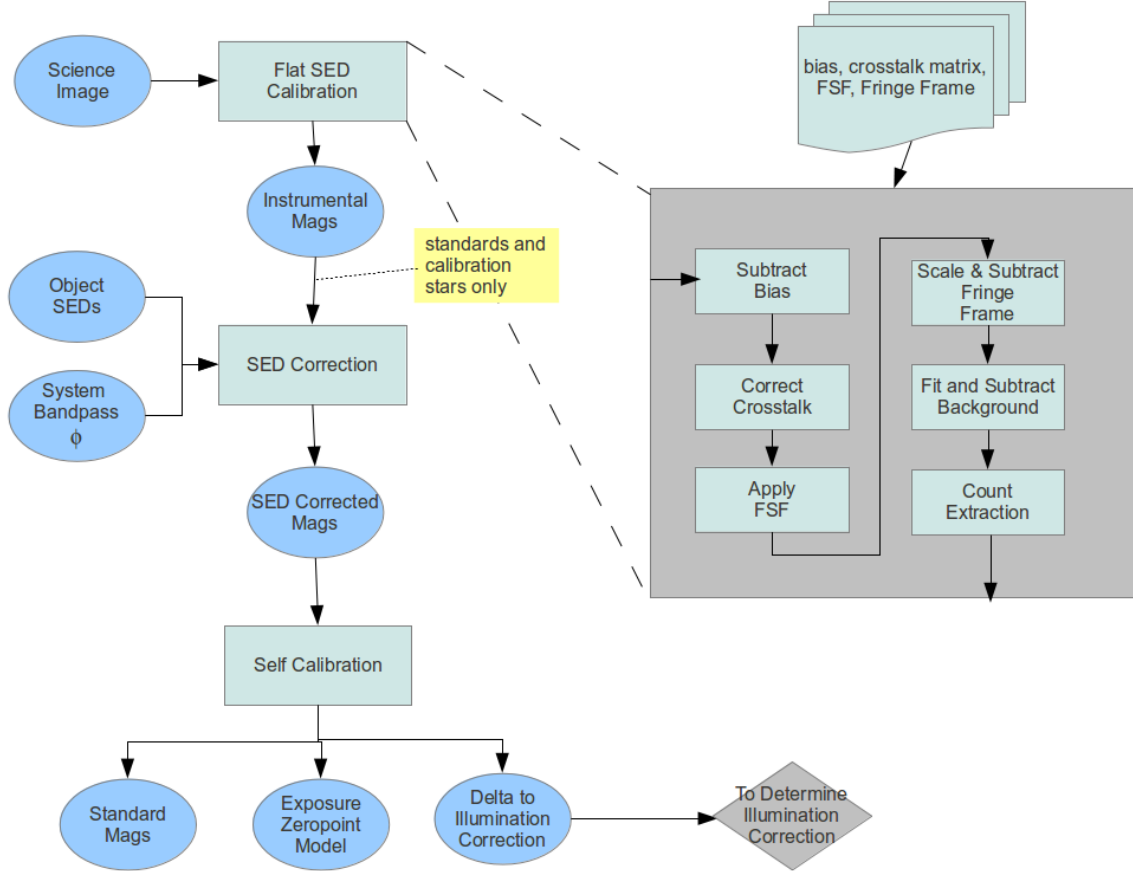These quantities are related through equations 14 and 14.

Figure 1: **The overall flow of the Data Release photometric calibration process.** The process consists of three main steps. In the first, Flat SED Calibration, science image pixels are processed to instrumental magnitudes as if all calibration object SEDs were flat ($F_\nu = const$). The second step, SED Correction, corrects the flat SED object counts to account for the real system bandpass and calibration object SEDs, generating corrected magnitudes. The final step, Self Calibration, solves a least squares system in the SED corrected magnitudes to yield the standard magnitudes for the calibration objects and a spatially dependent zeropoint correction for each exposure. Additionally, corrections to the illumination correction are calculated, for use in "Determine Illumination Correction" (Figure 2). Note that SED Correction and Self Calibration are performed only for calibration objects. General science objects are calibrated later, using the data products from the calibration process (Figure 4)
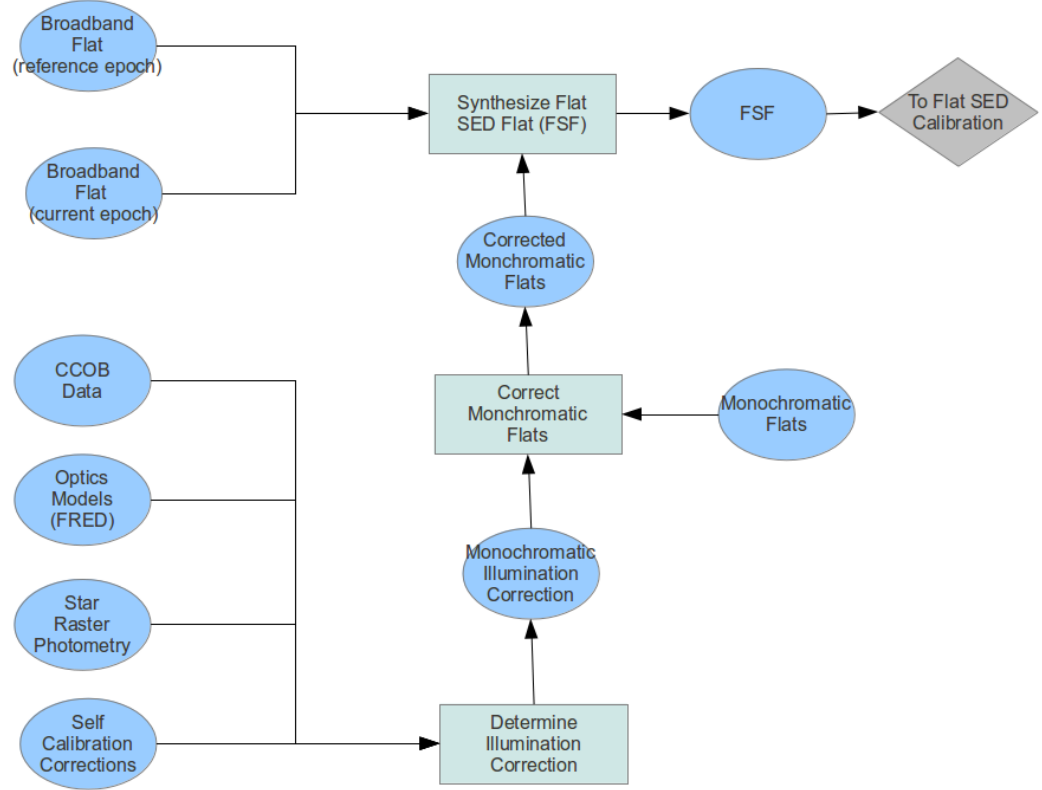
Figure 2: **Flat SED Flat Determination.** Determination of the flat SED flat (FSF) is of central importance. The initial step in the calibration process treats all objects as if their SED were flat. This is consistent only if the flatfield is that for a flat SED, as transmitted through a reference atmosphere. Since the illumination source for the actual broadband flat does not have the required SED, we cannot use it directly. Instead, we synthesize the required flat from the monochromatic flats. These flats as measured are contaminated by light which arrives from paths other than the direct path, such as ghosting. These effects are taken out by the illumination correction. Finally, the monochromatic flats are taken relatively infrequently, and will not reflect changes on shorter timescales, such as the appearance of new dust particles. We account for this by multiplying the synthesized FSF by the ratio of two broadband flats, one at the current epoch and one at the reference epoch, when the monochromatic flats were gathered.
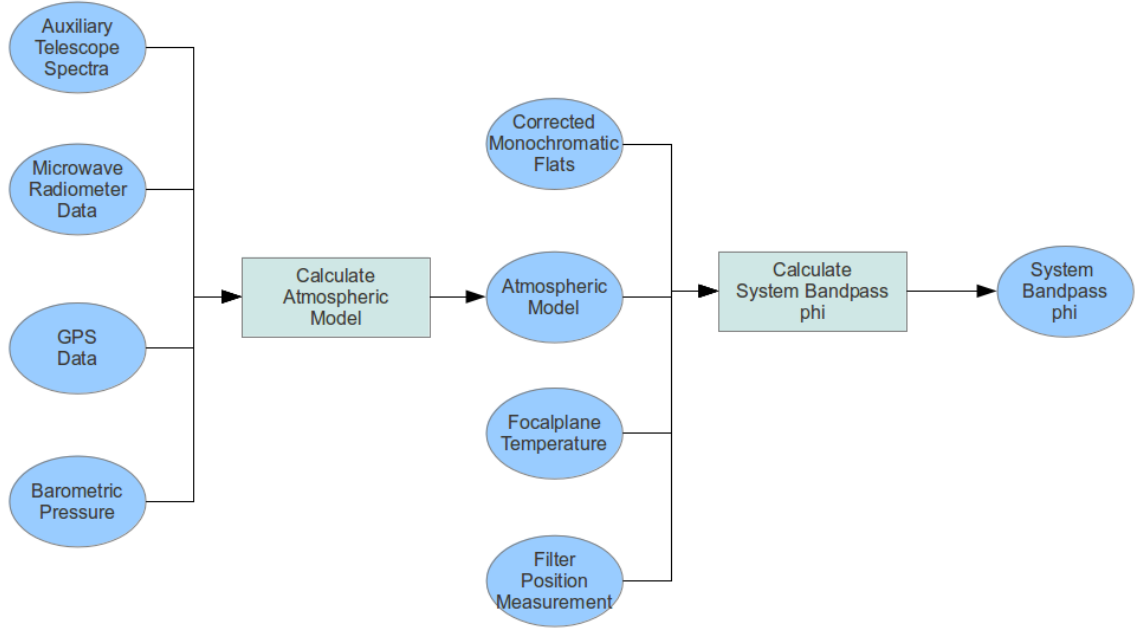
Figure 3: **System Bandpass Determination.** The system bandpass, ϕ, is determined for every exposure, and is a major output of the calibration process. It is the normalized product of the atmospheric bandpass and that of the telescope/camera system. The atmospheric bandpass is determined by fitting an atmospheric model to a set of measured atmospheric data. The bandpass of the telescope/camera system is measured by the corrected monochromatic flats, modified by current data from the camera system, principally focalplane temperature and the filter position.
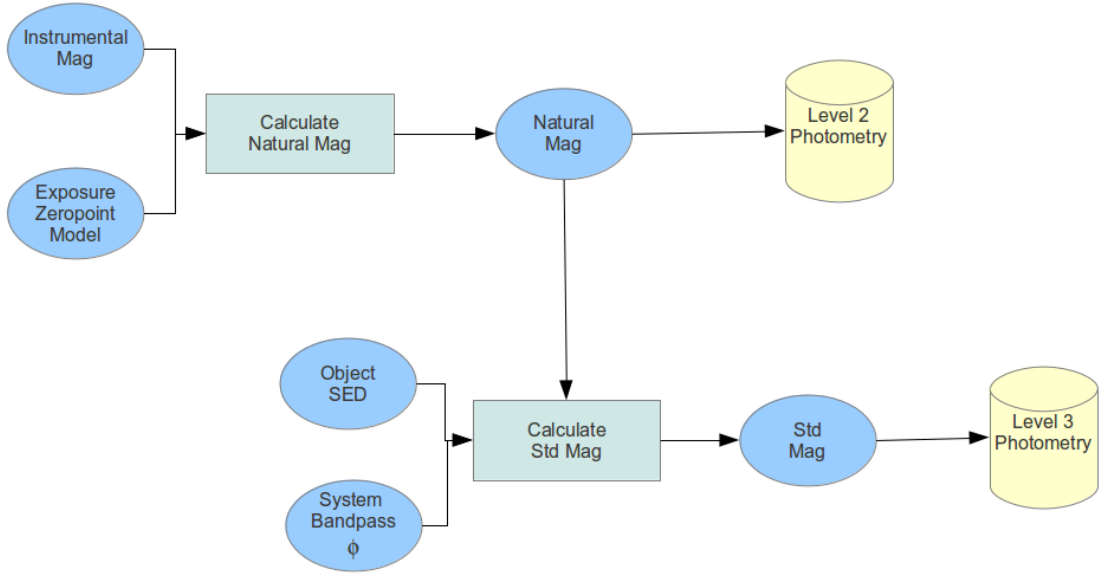
Figure 4: **Science Object Calibration.** Photometric calibration for science objects takes place in two stages. In the first, the natural magnitudes are calculated, using the zeropoint model for each exposure. These are stored in the Level 2 databases. The second, optional, stage, relies on knowledge of the object SEDs, which is an external input to the system, supplied by the user. The object SED, in conjunction with the system bandpass, ϕ, allows standard magnitudes to be calculated. These are considered a Level 3 data product

3.1. From Photons to Counts

We first consider how the photons from an astronomical object are converted into ADUs in the detector, paying attention to the various temporal or spatial scales for variability might arise in the LSST system to affect the final ADU counts.

Given $F_\nu(\lambda, t)$ – the specific flux[1] (flux per unit frequency) of an astronomical object at the top of the atmosphere – at a position described by (alt,az), the total flux from the object transmitted through the atmosphere to the telescope pupil is

$$F_\nu^{pupil}(\lambda, alt, az, t) = F_\nu(\lambda, t)\, S^{atm}(\lambda, alt, az, t), \tag{1}$$

where $S^{atm}(\lambda, alt, az)$ is the (dimensionless) probability that a photon of wavelength λ makes it through the atmosphere,

$$S^{atm}(\lambda, alt, az, t) = \mathrm{e}^{-\tau^{atm}(\lambda, alt, az, t)}. \tag{2}$$

Here $\tau^{atm}(\lambda, alt, az)$ is the optical depth of the atmospheric layer at wavelength λ towards the position (alt,az). Observational data (??) show that the various atmospheric components which contribute to absorption (water vapor, aerosol scattering, Rayleigh scattering and molecular absorption) can lead to variations in $S^{atm}(\lambda, t)$ on the order of 10% per hour. Clouds represent an additional gray (non-wavelength dependent) contribution to τ^{atm} that can vary even more rapidly, on the order of 2–10% of the total extinction at $1°$ scales within minutes (?).

Given the above $F_\nu^{pupil}(\lambda, alt, az, t)$, the total ADU counts transmitted from the object to a footprint within the field of view at (x, y) can be written as

$$C_b(alt, az, x, y, t) = C \int_0^\infty F_\nu^{pupil}(\lambda, alt, az, t)\, S_b^{sys}(\lambda, x, y, t)\lambda^{-1}d\lambda. \tag{3}$$

Here, $S_b^{sys}(\lambda, x, y, t)$ is the (dimensionless) probability that a photon will pass through the telescope's optical path to be converted into an ADU count, and includes the mirror reflectivity, lens transmission, filter transmision, and detector sensitivity. The term λ^{-1} comes from

---

[1]Hereafter, the units for specific flux (flux per unit are Jansky (1 Jy $= 10^{-23}$ erg cm^{-2} s^{-1} Hz^{-1}). The choice of F_ν vs. F_λ makes the flux conversion to the AB magnitude scale more transparent, and the choice of λ as the running variable is more convenient than the choice of ν. Note also, while $F_\nu(\lambda, t)$ (and other quantities that are functions of time) could vary more quickly than the standard LSST exposure time of 15s, it is assumed that all such quantities are averaged over that short exposure time, so that t refers to quantities that can vary from exposure to exposure.

the conversion of energy per unit frequency into the number of photons per unit wavelength and b refers to a particular filter, $ugrizy$. The dimensional conversion constant C is

$$C = \frac{\pi D^2 \Delta t}{4gh} \qquad (4)$$

where D is the effective primary mirror diameter, Δt is the exposure time, g is the gain of the readout electronics (number of photoelectrons per ADU count, a number greater than one), and h is the Planck constant. The wavelength-dependent variations in S_b^{sys} generally change quite slowly in time; over periods of months, the mirror reflectance and filter transmission will degrade as their coatings age. A more rapidly time-varying wavelength-dependent change in detector sensitivity (particularly at very red wavelengths in the y band) results from temperature changes in the detector, but only on scales equivalent to a CCD or larger. There will also be wavelength-dependent spatial variations in S_b^{sys} due to irregularities in the filter material; these are required by the camera specifications to vary (at a maximum) slowly from the center of the field of view to the outer edges, equivalent to a bandpass shift on the order of 1-2% of the effective wavelength of the filter. Wavelength-independent (gray-scale) variations in S_b^{sys} can occur more rapidly, on timescales of a day for variations caused by dust particles on the filter or dewar window, and on spatial scales ranging from the amplifier level, arising from gain changes between amplifiers, down to the pixel level, in the case of pixel-to-pixel detector sensitivity variations.

From equation 3 and the paragraphs above, we can see that the generation of counts $C_b(alt, az, x, y, t)$ from photons is imprinted with many different effects, each with different variability scales over time, space, and wavelength. In particular the wavelength-dependent variability (bandpass shape) is typically much slower in time and space than the gray-scale variations (bandpass normalization). These different scales of variability motivate us to separate the measurement of the normalization of S_b^{sys} and S^{atm} from the measurement of the wavelength-dependent shape of the bandpass.

3.1.1. Normalized bandpass response, $\phi_b(\lambda)$

This then leads us to introduce a 'normalized bandpass response function', $\phi_b^{obs}(\lambda, t)$, that represents the true bandpass response shape for each observation,

$$\phi_b^{obs}(\lambda, t) = \frac{S^{atm}(\lambda, alt, az, t)\, S_b^{sys}(\lambda, x, y, t)\, \lambda^{-1}}{\int_0^\infty S^{atm}(\lambda, alt, az, t)\, S_b^{sys}(\lambda, x, y, t)\, \lambda^{-1}\, d\lambda}. \qquad (5)$$

Note that ϕ_b only represents *shape* information about the bandpass, as by definition

$$\int_0^\infty \phi_b(\lambda) d\lambda = 1. \qquad (6)$$

Using $\phi_b^{obs}(\lambda, t)$ we can represent the (true, total) in-band flux of an object for each observation as

$$F_b^{obs}(t) = \int_0^\infty F_\nu(\lambda, t) \, \phi_b^{obs}(\lambda, t) \, d\lambda, \tag{7}$$

where the normalization of $F_b(t)$ corresponds to the top of the atmosphere. Unless $F_\nu(\lambda, t)$ is a flat $(F_\nu(\lambda) = \text{constant})$ SED, F_b^{obs} will vary with changes in $\phi_b^{obs}(\lambda, t)$ due simply to changes in the bandpass shape, such as changes with position in the focal plane or differing atmospheric absorption characteristics, *even if the source is non-variable.*

To provide a reported $F_b^{std}(t)$ which is constant for non-variable sources, we also introduce the 'standardized bandpass response function', $\phi_b^{std}(\lambda)$, a curve that will be defined before the start of LSST operations (most likely during commissioning). $\phi_b^{std}(\lambda)$ represents a typical hardware and atmospheric transmission curve, minimizing the difference between $\phi_b^{obs}(\lambda, t)$ and the standardized reported bandpass. Now,

$$F_b^{std}(t) = \int_0^\infty F_\nu(\lambda, t) \, \phi_b^{std}(\lambda) \, d\lambda, \tag{8}$$

is a constant value for non-variable sources.

Magnitudes provide an easy way to conceptualize the relationship between F_b^{obs} and F_b^{std}, provided that we define a 'natural magnitude'

$$m_b^{nat} = -2.5 \, log_{10} \left(\frac{F_b^{obs}}{F_{AB}} \right) \tag{9}$$

where $F_{AB} = 3631$ Jy. The natural magnitude, like F_b^{obs} will vary from observation to observation as $\phi_b^{obs}(\lambda, t)$ changes, even if the source itself is non-variable. The natural magnitude can be translated to a 'standard magnitude', m_b^{std}, as follows:

$$m_b^{nat} = -2.5 \, log_{10} \left(\frac{F_b^{obs}}{F_{AB}} \right) \tag{10}$$

$$= -2.5 \, log_{10} \left(\frac{\int_0^\infty F_\nu(\lambda, t) \, \phi_b^{obs}(\lambda, t) \, d\lambda}{F_{AB}} \right) \tag{11}$$

$$= -2.5 \, log_{10} \left(\left(\frac{\int_0^\infty F_\nu(\lambda, t) \, \phi_b^{obs}(\lambda, t) \, d\lambda}{\int_0^\infty F_\nu(\lambda, t) \, \phi_b^{std}(\lambda, t) \, d\lambda} \right) \left(\frac{\int_0^\infty F_\nu(\lambda, t) \, \phi_b^{std}(\lambda, t) \, d\lambda}{F_{AB}} \right) \right) \tag{12}$$

$$m_b^{nat} = \Delta m_b^{obs} + m_b^{std} \tag{13}$$

where Δm_b^{obs} varies with the *shape* of the source spectrum, $f_\nu(\lambda, t)$ and the *shape* of the bandpass $\phi_b^{obs}(\lambda, t)$ in each observation. Note that $\Delta m_b^{obs} = 0$ for flat (constant) SEDs, as the integral of $\phi_b(\lambda)$ is always one. For non-variable sources, m_b^{std} will be non-variable as it represents the throughput in a standardized bandpass, $\phi_b^{std}(\lambda)$.

The natural and standard magnitudes can be tied back to the counts produced by the system by adding the correct zeropoint offsets. As Δm_b^{obs} removes all wavelength dependent variations in m_b^{std},

$$m_b^{std} = -2.5\, log_{10}(C_b^{obs}) - \Delta m_b^{obs} + Z_b^{obs} \tag{14}$$

the zeropoint correction here, Z_b^{obs}, contains only gray-scale *normalization* effects, such as variations due to the flat field or cloud extinction.

3.1.2. Perturbations to the System Bandpass

The normalized system bandpass will vary from exposure to exposure due to a myriad of effects. The major ones are:

- Atmospheric transmission variations. The major wavelength-dependent sources of atmospheric absorption, Rayleigh scattering from molecules, ozone, water vapor, and aerosols, all vary in time and space, with widely varying temporal and spatial scales. Even in the absence of intrinsic variation in the atmosphere, of course, the bandpass varies due to changing airmass. This latter effect is compensated for in traditional photometric calibration, but the others are generally ignored

- Long term variations in the throughput of the optical path due to contamination

- Changing detector quantum efficiency, particularly in the y-band, due to varying focal plane temperature

- Shifts in filter position with respect to the system optical axis, due to positioning jitter and gravity sag

It bears repeating that every perturbation in general affects both the zeropoint, through the gray component of the perturbation, and the shape of the system bandpass, through the wavelength-dependent component. The gray component is removed by the self calibration process, while the wavelength-dependent component must be separately characterized and removed (see Figure 1). We are concerned here only about the latter effect, and discuss it for each of the above categories.

3.1.3. Effects of Atmospheric Variations

The main components of wavelength-dependent atmospheric extinction are Rayleigh scattering from molecules; water vapor; ozone; and aerosols. Rayleigh scattering extinction

is directly proportional to barometric pressure at the surface. As is well known from looking at surface pressure charts, away from weather fronts the pressure varies significantly on timescales of hours or more and spatial scales of hundreds of km. Variations can be much more rapid in the vicinity of fronts. In any case, this component can be compensated for very accurately just by measuring the barometric pressure, and we do not further consider it here. The other components are not so easily measured, and in the case of water vapor and aerosols, can display complex patterns of variability. As a case in point, consider Figure 5, which shows a time-altitude profile of aerosol variations at a site in the US. Although the site is quite different from Cerro Pachon (CP), there are nonetheless significant variation of aerosol extinction at altitudes above 3000m on time scales well under an hour, and we should expect similar variations at CP.

Water vapor shows even more pronounced variations. Figures 7, **??**, and 8 give three different perspectives on historical water vapor variability in the vicinity of CP. There are broad patterns in space (the E-W gradient), and in time (the regular seasonal variations). There are large variabilities on top of these, amounting to several mm of PWV, which can occur in hours or less. The biggest effect of water vapor is in the y-band, since it contains a strong water band (Figure **??**). Figure **??** shows the magnitude of the effect for a star with g-i=-0.5. The 4mm variation in PWV shown in Figure **??** would lead to a 3mmag error in calibration of y photometry, if not compensated for. Moreover, the variation is strongly dependent on star color (Figure **??**), so the increased scatter in photometry for an ensemble of stars will be significantly greater.

3.1.4. Throughput Variations Due to Contamination

3.1.5. Variations in Detector Quantum Efficiency

3.1.6. Throughput Variations Due to Filter Position Shifts

3.1.7. Putting it All Together

Examples of the Δm_b^{obs} due to variations in the shape of the hardware and atmospheric response curves are shown in Figure 9 and Table 1. Two main sequence stellar models (**?**) – one with temperature 35000K (blue) and one 6000K (red) – were combined with three different atmospheric response curves (with airmass X=1.0 with minimal H_2O vapor, X=1.2 with a nominal amount of H_2O (the 'standard'), and X=1.8 with a large H_2O vapor content) and two different hardware response curves (one 'standard' and one shifted in wavelength by 1%) to illustrate the resulting changes in observed natural magnitudes. In
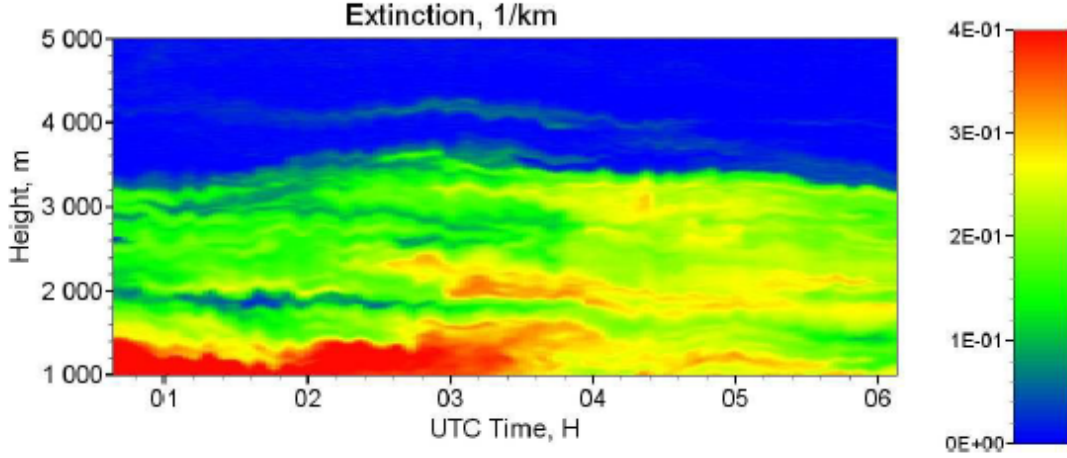
Figure 5: Lidar measurements of aerosol extinction at 355nm over a single night near Greenbelt, MD (**?**). Cerro Pachon is, of course, a different environment, and is at an altitude 2700m, removing much of the variability. Even above that altitude, however, significant variation on rapid time scales remains.

Figure 10, the $X = 1.8$ atmospheric response is combined with a 1% shift (the maximum allowed in the filter manufacturing specification from center to edge) in filter bandpass, thus altering the hardware response, for many main sequence Kurucz models spanning a range of $g - i$ colors; the resulting changes in natural magnitudes are plotted. These examples demonstrate that the scatter in natural magnitudes induced by expected atmospheric and hardware transmission curve shape changes alone (without any gray-scale changes) can be larger than the SRD repeatability requirements would permit. Adding variations in the gray-scale normalization due to the hardware response and cloud extinction will increase the scatter in the observed magnitudes even further.

3.2. From Counts to Photons

The previous section laid out the origins of ADU count variability from one observation to another. Now we will consider how we can, in practice, acquire the information necessary to convert a particular observed ADU count to a measurement of $F_\nu(\lambda, t)$ above the atmosphere for a particular object. This requires measuring and then compensating for the
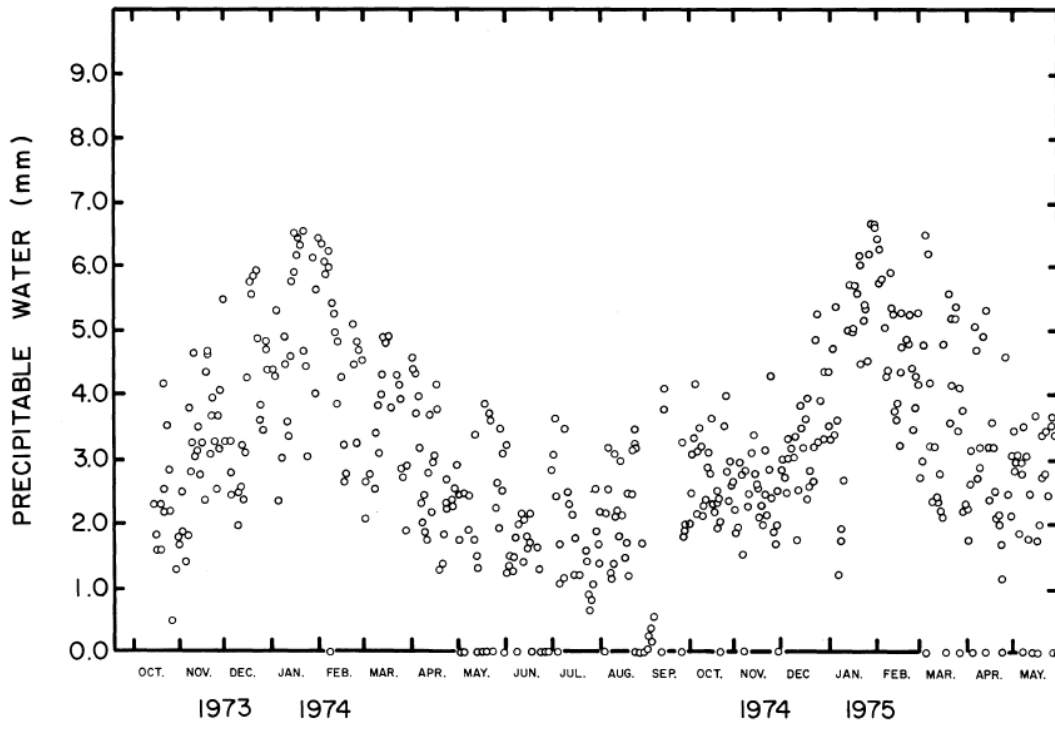
Figure 6: Three years of PWV measured at CTIO ((**?**)), based on the depth of the 1.87 μm line to the Solar continuum at 1.65 μm.
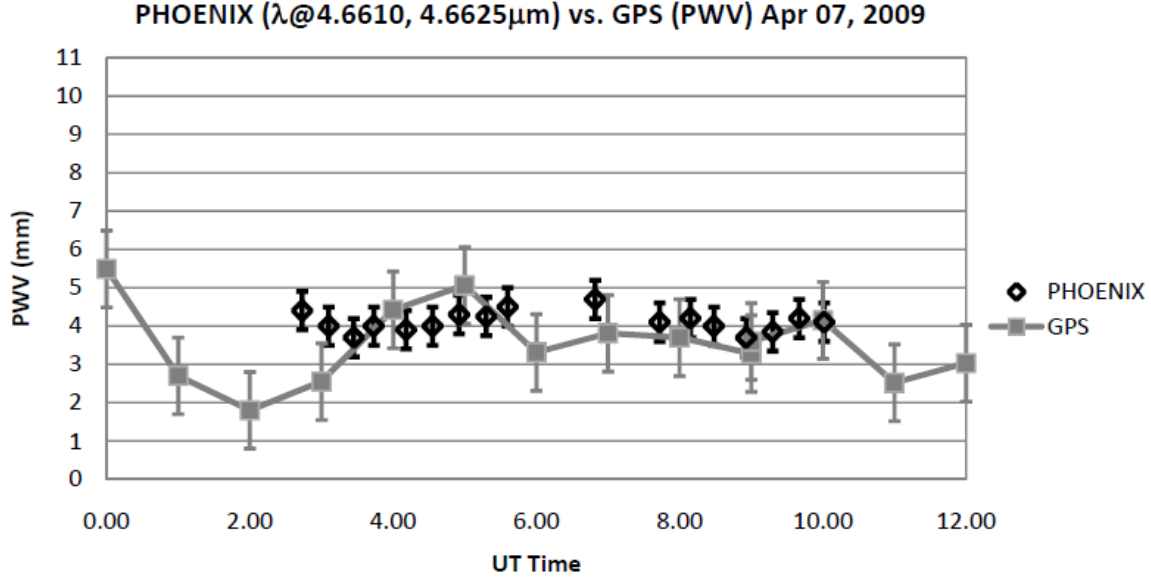
Figure 7: PWV measured on a single day at Gemini S (?). Two techniques were used, GPS and Phoenix, an IR spectrograph, and the data are in good agreement. Note the decline of approximately 4 mm over a period of two hours. This is a case where use of a single average atmosphere for a whole night would give poor results, especially in the y-band.

variations in $S^{atm}(\lambda, alt, az, t)$ and $S_b^{sys}(\lambda, x, y, t)$. Let us first consider measurement of the variations in the hardware throughput curve, $S_b^{sys}(\lambda, x, y, t)$.

To measure the wavelength-dependent hardware response curve as a function of position in the focal plane, we will use a dome-screen system that is capable of producing narrow-band light over a range of wavelengths, producing a data cube of 'narrow-band flat fields'. After applying the monochromatic illumination correction (see Section ??) and applying the normalization at each wavelength from the photodiode monitors (see Section XX), this data cube records (up to an overall normalization constant) $S_b^{sys}(\lambda, t)$ at each x,y location in the focal plane. This data cube of narrow-band flats is used to construct a synthetic flat field by combining the individual narrow-band flats according to a chosen spectral energy distribution. Since the first stage of the calibration process, that which processes the actual pixels, assumes that sources have flat SEDs, we construct our synthetic flat with a flat SED propagated through a mean model atmosphere to the entrance pupil of the telescope. We call this flat the 'flat spectrum flat' (FSF).

Generation of the entire data cube of narrow-band flats is too time-consuming to complete on a daily basis. Instead, the full narrow-band flat field scan will only be repeated on a time interval adequate for measurement of the more slowly variable components of $S_b^{sys}(\lambda, t)$,
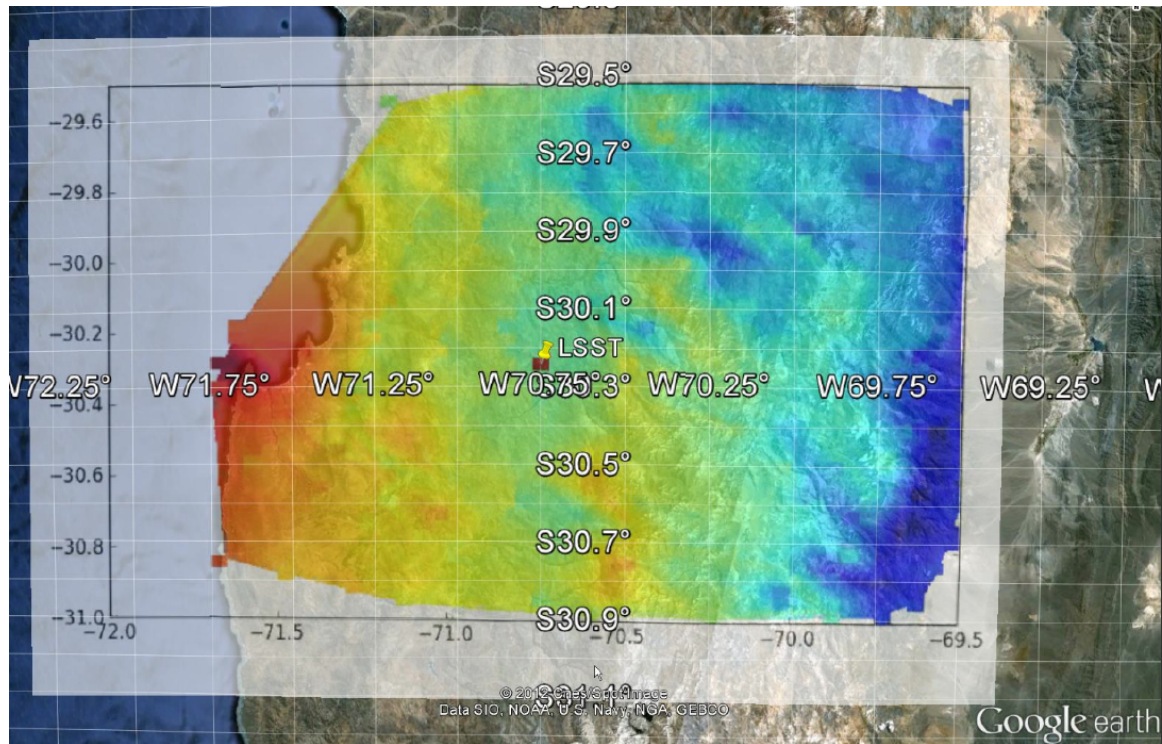
Figure 8: PWV measurement from the MODIS satellite at one time in the region around Cerro Pachon. The color scale ranges from 4.3 mm (blue) to 7.6 mm (dark red). Note the strong E-W gradient in PWV.
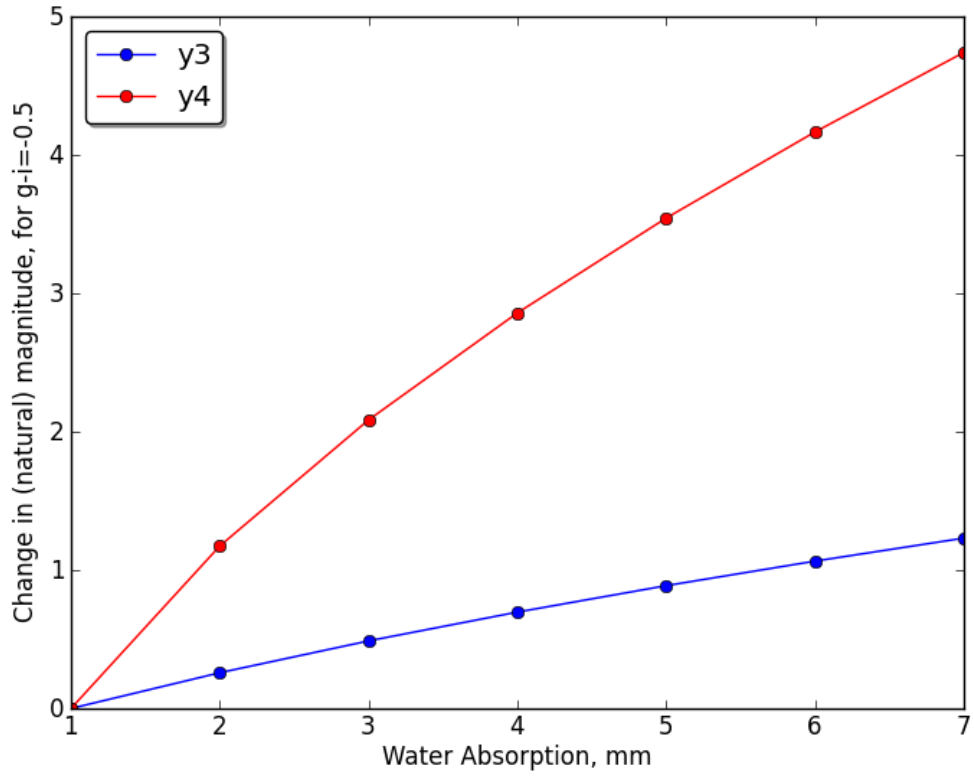
Figure 9: Change in natural magnitude in the LSST y3 and y4 (baseline) filters as a function of PWV for a star with g-i=0.5 mag. The units on the y-axis are mmag.
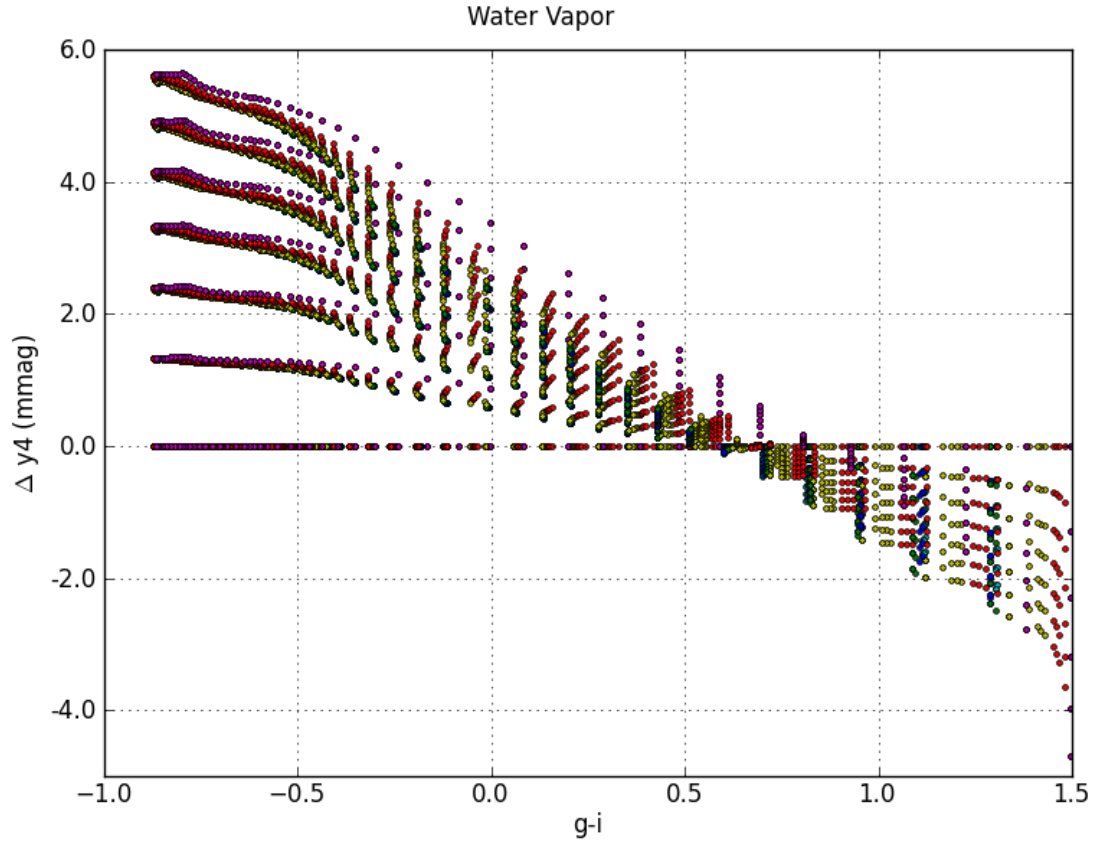
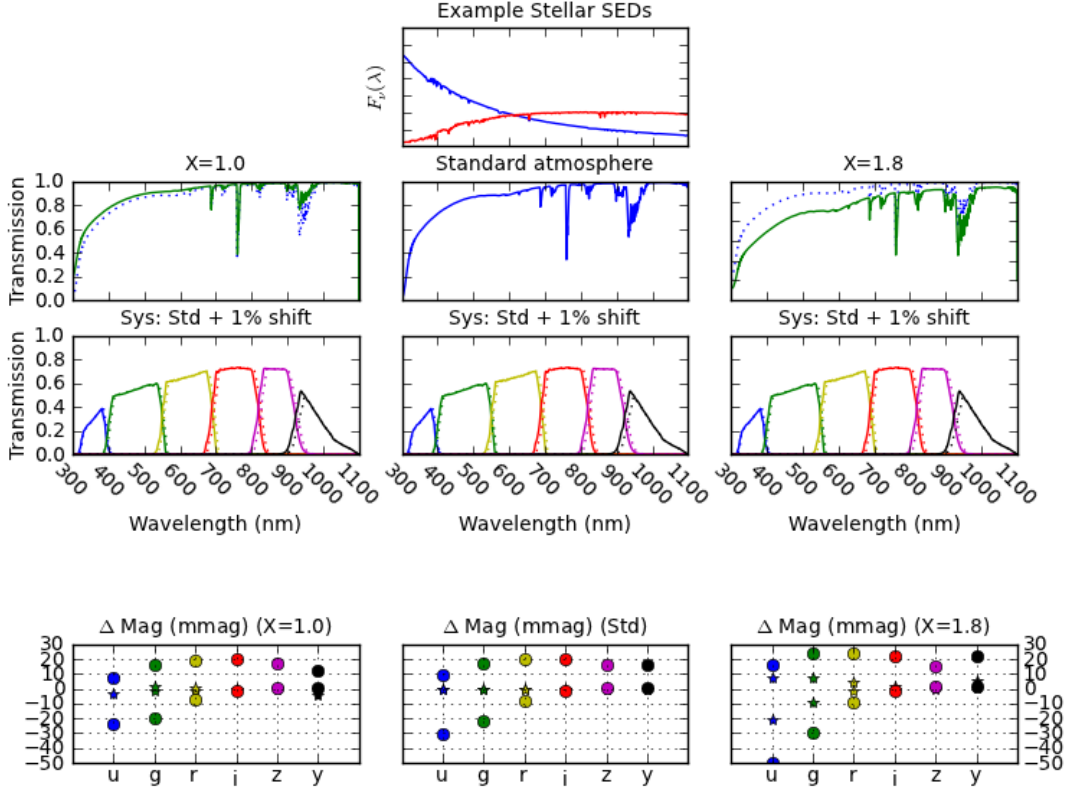Figure 10: Variations in y4 photometry with changing water vapor for a range of star colors

Figure 11: Δm_b^{obs} **due to variations in hardware and atmospheric bandpass shape.** Two main sequence Kurucz model stars, one blue (35000 K, approximately O type) and one red (6000 K approximately G type), were used to generate natural magnitudes (see Eqn 9) using three different atmospheric transmission profiles and two different hardware transmission profiles. The stellar flux profiles are shown in the top center panel, while the atmospheric transmission functions ($S^{atm}(\lambda)$) are shown across the second row and the two hardware transmission profiles ($S_b^{sys}(\lambda)$) are duplicated across the third row. The atmospheric transmission profiles correspond to an airmass X=1.0, 1.2 and 1.8 (from left to right), with variable atmospheric absorption components. The X=1.0 atmosphere is very similar but not identical to the current LSST default X=1.2 atmosphere throughput curve, which is used as 'standard' here. The hardware transmission profiles consist of a 'standard' profile (matching the LSST current expected values) and version where the filter throughputs have been shifted by 1% of the effective wavelength of each filter (consistent with the shift expected near the spatial edge of each filter). The final row demonstrates the changes in observed magnitudes produced by the X=1.0, 'standard' and X=1.8 atmospheres (left to right, respectively), combined with both the 'standard' hardware transmission (represented by the star points) and the +1% shifted hardware transmission (represented by the filled circles) for both the red and blue stars. The exact differences in magnitudes resulting from this calculation are listed in Table 1.
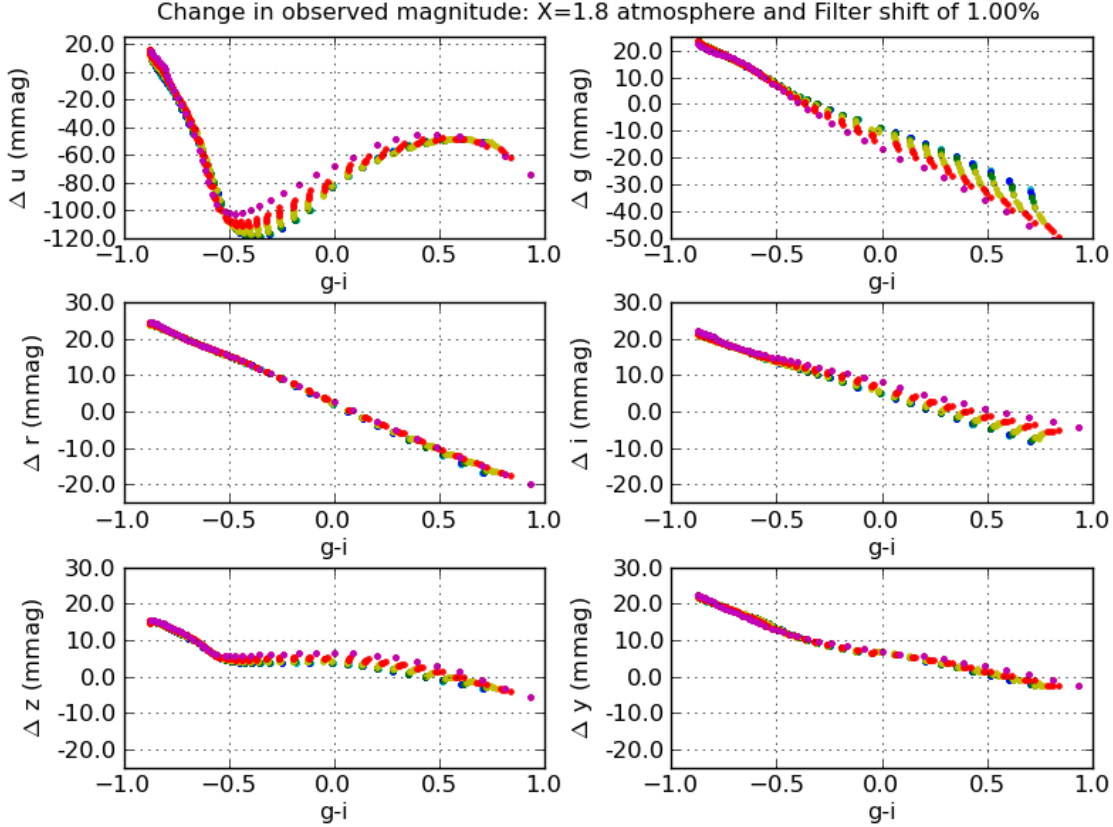
Figure 12: Δm_b^{obs} **due to a change in bandpass shape corresponding to a filter shift of** 1% **and an** $X = 1.8$ **atmosphere.** 850 Kurucz models with temperatures between 5000K and 35000K and metallicity indexes between -5.0 and 1.0 (solar) were combined with a standard system response (standard atmosphere and standard hardware bandpasses), then with a total system response where the atmosphere was replaced by an X=1.8 atmosphere and the filter component of the hardware transmission was shifted by 1% (as in Fig 9). The points in each plot are color-coded by metallicity, in steps of 1 dex between -5.0 (blue) to 1.0 (magenta). It can be seen that the relationship between Δm_b^{obs} and $g - i$ can be parameterized, although generally not with a simple linear relationship. In some cases (such as seen in the Δu and Δg panels), calculating Δm_b^{obs} to SRD levels may require more than a simple $g - i$ color, but this is then primarily a function of metallicity (which is possible to determine given the $u - g$ color in addition to the $g - i$ information).

Table 1:: Δm_b^{obs} **due to variations in system and atmospheric bandpass shape (see also Fig 9). The first two rows show the baseline ('standard') magnitude of the star. All other rows show the** *change* **in magnitude (in mmag) due to the variations listed at left. Any value larger than 5 mmag would be larger than the RMS scatter allowed by the SRD.** *TODO color-code values larger than 5 mmag*

Bandpass	star	u (mag)	g	r	i	z	y
Std (X=1.2) atm, std sys	red	21.472	20.378	20.000	19.911	19.913	19.913
Std (X=1.2) atm, std sys	blue	19.102	19.503	20.000	20.378	20.672	20.886
		Δu (mmag)	Δg	Δr	Δi	Δz	Δy
Std (X=1.2), +1% sys shift	red	-31	-22	-8	-2	1	1
Std (X=1.2), +1% sys shift	blue	9	17	20	20	16	16
X=1.0, std sys	red	7	2	0	0	-0	-1
X=1.0, std sys	blue	-3	-1	-1	-0	1	-4
X=1.0, +1% sys shift	red	-24	-20	-8	-1	1	0
X=1.0, +1% sys shift	blue	7	16	19	20	18	12
X=1.8, std sys	red	-21	-10	-2	-0	0	1
X=1.8, std sys	blue	8	8	4	2	-1	6
X=1.8, +1% sys shift	red	-50	-30	-10	-2	1	2
X=1.8, +1% sys shift	blue	16	24	24	22	15	22

approximately monthly (but to be determined during commissioning). This measurement is discussed in detail in section **??**. Since the system response can change on shorter timescales, principally due to a changing population of dust particles on optical surfaces, we correct the FSF by multiplying by the ratio of two broad-band flats, one at the current epoch and one at the reference epoch when the narrow-band flats were acquired.

As mentioned above, before these flat fields (both the broadband and the narrow-band flats) can be used to measure S_b^{sys}, they must be modified to correctly produce *photometrically* uniform measurements of stars of a defined reference SED across the field of view. This correction is called the 'illumination correction'. The illumination correction must correct the observed flat fields for effects resulting from non-uniform illumination of the dome screen, for ghosting caused by internal reflections in the camera, and for the presence of stray or scattered light arriving in the focal plane on path that are not part of the optical design (such as light bouncing from the dome floor or glinting off a filter holder). See figures **??** and **??** for a visual example of the illumination correction and its importance to image processing. The illumination correction will be wavelength dependent; for the narrow-band flat fields, an illumination correction for each wavelength must be generated. The illumination correction

(including ghost corrections) will be generated by combining measurements of bright, dense star fields rastered across the field of view during specialized observing sequences and further corrections generated by the self-calibration stage (discussed below in section **??**). For the narrow-band flat fields, forward modeling will be useful in generating the illumination correction. This may include FRED (**??** modeling, constrained with measurements from the 'camera calibration optical bench' (CCOB - see a brief description in Section D). Further corrections will be again generated by the self-calibration stage. The illumination correction is expected to be stable with time and will be remeasured only if components in the optical path of the telescope are altered.

Next, considering $S^{atm}(\lambda, alt, az, t)$, we will again separate the measurement of the shape of the atmospheric response and the measurement of normalization of the transmission. The currently available data is still incomplete, but suggests that the wavelength-dependent variations in $\phi^{atm}(\lambda, t)$ change smoothly over spatial scales larger than the field of view and over several minutes. By using an auxiliary telescope equipped with a spectrograph to observe bright stars with known SEDs, we can measure atmospheric absorption at a variety of positions in the sky every 5–10 minutes throughout the night. These observations are used as constraints for MODTRAN atmospheric models, generating representations of the atmospheric throughput in the form of a set of absorption components as a function of alt, az, t. These components can be interpolated in time and space to generate a wavelength-dependent atmospheric absorption profile, $\phi_b^{atm}(\lambda, alt, az, t)$, for each observation. This process is discussed in detail in section **??**.

In order to correct for the more rapid gray-scale variations in the relative normalization of $S^{atm}(alt, az, t)$ due to cloud extinction, we must use the observations of calibration stars in the images themselves, as observations ((**?**), (**?**)) suggest that cloud extinction can vary by 0.01 magnitudes on the scale of a CCD on timescales as fast as a few minutes. This 'self-calibration' procedure could be thought of as creating a massive calibration 'standard' star catalog, where the calibration stars are all of the non-variable, main-sequence stars in the science images; the main difference is that the true magnitudes of the calibration stars have to be bootstrapped from the many different observations of the survey. For every calibration star (main sequence star identified as non-variable, isolated, and in the desired magnitude range), corrections for $\phi_b^{sys+atm}(\lambda, t)$ must be applied to produce a standardized magnitude, m_b^{std}, then in the self-calibration procedure we minimize the difference between the standardized magnitude and a model magnitude,

$$\chi^2 = \Sigma_{ij} \left(\frac{m_{b,ij}^{std} - m_{b,ij}^{model}}{\sigma_{b,ij}^{std}} \right)^2 \tag{15}$$

where the model magnitude is derived from the best-fit 'true' magnitude of the calibration

star and a model describing how we expect the magnitude to vary from observation to observation. In the simplest self-calibration plan, this model simply consists of a normalization constant (zeropoint offset) for a 'patch' equivalent to the size of a CCD,

$$m_{b,ij}^{model} = m_{b,i}^{best} - \delta z_{b,j}. \tag{16}$$

This produces best-fit magnitudes for the calibration star catalog as well as zeropoint offsets (normalization constants) for each CCD in every observation, allowing us to correct for atmospheric extinction on the scale of a CCD. By adopting a more complex model, this procedure can also correct for variations in the relative normalization of the total system throughput beyond those contributed by cloud extinction (such as remaining errors in the illumination correction for the broadband and narrow-band flat fields), but is generally limited by the number of stars and number of observations of each star that are obtained. A CCD size patch provides about 100 stars per patch, allowing good signal to noise when determining cloud extinction which varies from observation to observation. Using this self-calibration procedure, It may be possible to determine longer term term effects (such as the illumination correction) down to scales approximately equivalent to the PSF. This is similar in nature to the ubercal method applied to SDSS in **?**, and more recently DLS (**?**) and PanSTARRS-1 (**?**).

Repeating Equation 14 above, adjusting *obs* indexes to *meas* to reflect the difference between the true and measured quantities,

$$m_b^{std} = -2.5\,log_{10}(C_b^{meas}) + \Delta m_b^{meas} + Z_b^{meas} \tag{17}$$

we can relate the terms in this equation to the corrections just described above. Δm_b^{meas} originates from the difference between $\phi_b^{meas}(\lambda, t, x, y)$ and $\phi_b^{std}(\lambda)$ convolved with the source SED, and thus it depends on the shape of the total system response as well as the shape of the source SED. Δm_b^{meas} will be calculated by combining a series of model SEDs with $\phi_b^{meas}(\lambda, t, x, y)$ at various locations in the focal plane, creating a lookup table of values to apply to measured magnitudes. For many sources (but not calibration stars), LSST will simply assume that the source has a flat SED, at which point the Δm_b^{meas} values become zero, although users may create their own SED and correction tables based on their knowledge of the true SED (see Appendix C). The Z_b^{meas} zeropoint offset comes from any normalization constants generated by the self-calibration procedure (in the simple model, just the $\delta z_{b,j}$ in equation 16 above).

These standard magnitudes are calibrated for variations in the observed bandpass shape (where applicable) and relative normalization, thus are directly comparable from one observation to the next. However, they are not yet tied to an external physical scale or from one

filter band to another, and thus only define an internally calibrated LSST magnitude in a particular filter.

To fulfill SRD requirements 3 and 4, these internally calibrated natural magnitudes must also be tied from one filter band to another, and then tied to an absolute external physical scale. For this, a further set of measurements is needed. In all filters, a set of spectrophotometric standards must be observed, and calibrated using the steps described above. Then the known SED is combined with the standard bandpass shape to generate synthetic color photometry. The synthetic colors are then compared with the calibrated measured standard magnitudes to calculate Δ_{b-r}, the corrections needed to tie measurements in each filter together (referenced to r band). At this point, only one final measurement is necessary to tie the entire system to an external physical scale: an r band LSST natural magnitude measurement of an absolutely calibrated source on a photometric night. Although in theory these last two steps could be done with a single externally calibrated object, on a single photometric night, a larger set of external reference objects with well known AB magnitudes will be used to reduce systematic errors. This defines an AB magnitude,

$$m_b^{AB} = m_b^{std} + \Delta_{b-r} + \Delta_r \qquad (18)$$

which can be compared to absolute physical flux scales.

The sequence for photometric calibration is then: **TODO turn this into a table**

1. Acquire a broadband flat in each filter at the start and end of each observing night. Generate a full, wavelength-dependent illumination correction for the flats on a much longer time interval (timescale to be determined, but much longer than monthly). Apply the appropriate illumination correction to the broadband flat. Apply flat field to images directly.

2. After remaining image processing (bias correction, fringe correction, etc) extract ADU counts of sources from images.

3. Acquire the data cube of narrow-band flat field images, approximately monthly. Apply wavelength-dependent illumination correction. Measure $\phi_b^{sys}(\lambda, t, x, y)$.

4. Acquire spectra of known stars roughly every 5–10 minutes throughout each night, fit for atmospheric absorption coefficients and generate $\phi_b^{atm}(\lambda, t)$ for each science images.

5. Combine ϕ_b^{atm} and ϕ_b^{sys} with a range of model SEDs to create lookup tables for Δm_b^{meas} for various locations in the focal plane.

6. At appropriate intervals (such as at Data Releases), run the self-calibration procedure, applying Δm_b^{meas} to stars chosen for self-calibration procedure and minimizing χ^2 from equation 15.

7. Apply appropriate Z_b^{meas} (and potentially Δm_b^{meas} values) to all objects in Data Release catalog, producing standardized magnitudes.

8. Apply measured corrections Δ_{b-r} and Δ_r, producing absolutely calibrated magnitudes.

This results in calibrated m_b^{AB} values in a standardized bandpass shape, with above-the-atmosphere fluxes.

4. Fixing LSST to an external scale

The next two subsections describe how the internally calibrated natural magnitudes, independently calibrated in each filter bandpass, are fixed to an external scale such that the flux in a single band can be compared to the flux in another filter band (SRD requirement 3) and that the flux in a particular filter band can be compared to an absolute external system (SRD requirement 4). This is equivalent to determining Δ_{b-r} and Δ_r from Eqn 18.

4.1. Band to band (color)

The band to band calibration for each filter b (the Δ_{b-r} values) will be determined by measuring the flux from one or more celestial objects whose physics are believed to be well understood. In principle, a single object with known colors would be sufficient, however many objects across the LSST footprint will be used to evaluate possible systematic effects in the internal calibration process.

Hot hydrogen (DA) and helium (DB) white dwarf stars have simple atmospheres that are reasonably well understood (model colors are currently reliable to about 0.01 magnitudes). It is estimated that there will be $\approx$ 100/10 DA/DB WD stars with $r < 24$ in each LSST image at the South Galactic Pole. Although in theory only one WD with high resolution spectroscopy would be required to calibrate colors for the entire survey, on the order of 100–1000 across the sky will be used to search for systematic effects. Catalogs of WD stars visible from Cerro Pachon have been constructed (??), and a 'white dwarf calibration system' has been developed (?). The locus of main sequence stars in color-color space is also reasonably well understood and has been used to calibrate photometry with success in previous surveys

(**??**). The use of the main sequence stellar locus in addition to WD stars will provide a valuable check on systematic effects that may arise from using (primarily) white dwarfs in the determination of $\phi^{atm}(\lambda, alt, az, t)$, as white dwarfs are bluer than most of the main sequence stars used for the bulk of the remainder of the calibration procedures. Additional checks on the quality of color calibration will be based on color residuals when determining photometric redshifts for galaxies. Analyzing these residuals as a function of galaxy brightness and color, and across the LSST footprint, will yield detailed quantiative estimates of the calibration quality. Although in theory one well-measured standard is all that would be necessary to determine Δ_{b-r} values for each bandpass, in practice having multiple standard with varying colors will serve as a check on systematics and provide estimates of the calibration uniformity throughout the survey.

The values for Δ_{b-r} will be determined by generating model m_b^{std} values for each band-band calibration object, then minimizing

$$\chi^2 = \Sigma_i \left(\frac{(m_{b,i}^{std} - m_{r,i}^{std})^{meas} - (m_{b,i}^{std} - m_{r,i}^{std})^{model}}{\sigma_{b-r,i}} \right)^2 . \tag{19}$$

This comparison can be done using subsets of objects from low Galactic extinction regions, and then bootstrapping to the entire sky to check for systematic effects.

4.2. Single bandpass to external flux system (absolute scale)

After determining the band to band calibration, there is a one further value required to calibrate the entire system to an absolute flux scale: Δ_r. This could again be determined using a single object with a well-known flux and spectral energy distribution, however multiple external calibrators provide a valuable check on systematic effects.

Several WDs in the Northern hemisphere have been very precisely calibrated with HST STIS measurements (**?**) and it should be possible to obtain similar HST measurements of one or more targets for use in the Southern hemisphere. Identification of these targets has not yet been completed. Nevertheless, as a result of calibration efforts to support the SDSS-II SNe survey, the absolute calibration of the SDSS Stripe 82 region in the r band is believed to be accurate at the 0.01 mag level (**?**). **TODO Tim will update with Abi white dwarf standards details**

Another route to calibrating to an external flux system is to use standards from Gaia. These will have the advantage of being numerous and widely spread across the sky, with a useful overlapping magnitude range between $r = 16$ to $r = 20$. The magnitude measurements

of stars calibrated with the LSST calibration procedure described in this document can be transformed to synthetic magnitudes in Gaia's bandpasses and compared to Gaia measurements. **TODO Tim will update with more information on Gaia**. This comparison across the LSST footprint and as a function of stellar brightness and color will provide a powerful independent test of the quality of LSST photometric calibration.

5. Calibration Hardware

5.1. Flat Field Illumination System

The dome screen projector is an array of projectors mounted in the dome of the LSST enclosure, specially designed to provide very uniform illumination to the LSST étendue (the incoming aperture of the telescope, taking into consideration the desired angle of the incoming light) while minimizing any light straying beyond the étendue. In addition, the dome screen will be able to project both broadband and tunable narrow-band (essentially monochromatic) light sources, providing both broadband (broadband) and narrow-band flat fielding capabilities. More details of the narrow-band flat field capabilities are provided in section **??**. The dome projector system is different from a traditional dome screen in that the 'screen' is a series of light sources, rather than a screen reflecting a single light source.

For both broadband and narrow-band flat field flat fields, the projectors are designed to fill the LSST étendue with a uniform illumination smoothly varying by less than 1% across the camera focal plane (corresponding to less than 10% variability across the projector surface) and less than 0.25% on scales smaller than 0.5° (a little larger than the size of a CCD). The projectors will also be designed to limit the extent of light emitted outside the étendue seen by the camera to reduce stray light in the flat fields (**?**). The broadband light source can be tuned to have any chosen spectral profile; this will be chosen during commissioning. For simplicity in discussing the next few sections, let us assume that this is a flat $F_\nu(\lambda)$ profile.
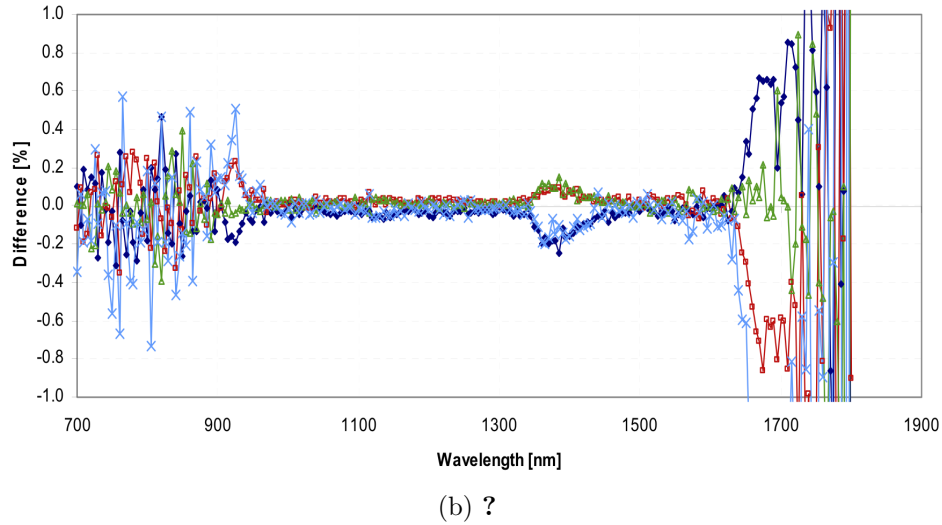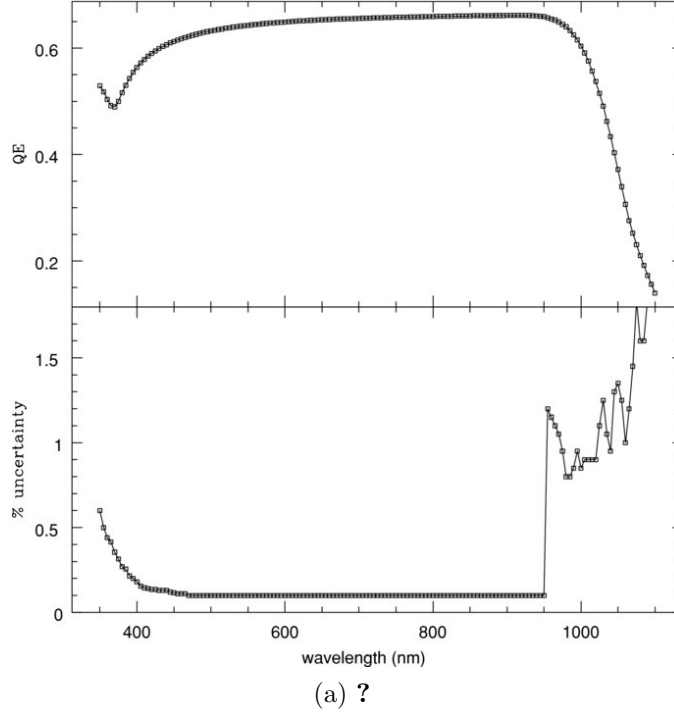
(a) **?**

(b) **?**

Figure 13: **Quantum efficiency curve and fractional uncertainty for NIST-calibrated photodiode, from ? and ?.** Panel 11a: Between 400 and 900 nm, calibration methods already in use in test systems indicate photodiode accuracy is better than 0.1%, as in the bottom part of this panel. The sudden decrease in calibration accuracy below 900 nm is due to calibration methods used by NIST in 2005. Panel 11b: More recent photodiode calibration efforts by **?** show better than 0.1% accuracy can be achieved to beyond 1200 nm, the limit of detector response for LSST, as shown here in the response curves resulting from multiple scans of a single source using the same photodiode.
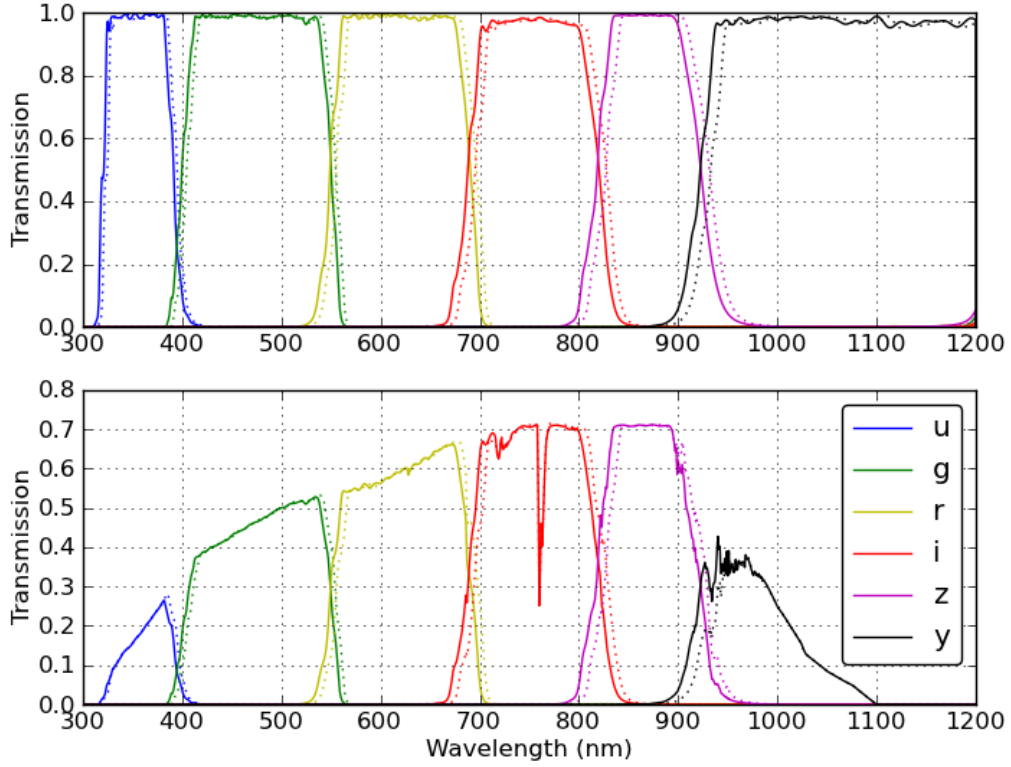
Figure 14: **Baseline filter curves and a potential (1% of the central wavelength) shift due to nonuniformity in the filter bandpass.** The solid lines indicate standard filter bandpasses (top panel: filter alone, bottom panel: filter plus standard mirror, lens, detector and atmosphere response curves) while the dashed lines indicate the same bandpass shifted redward by 1% of the central wavelength.
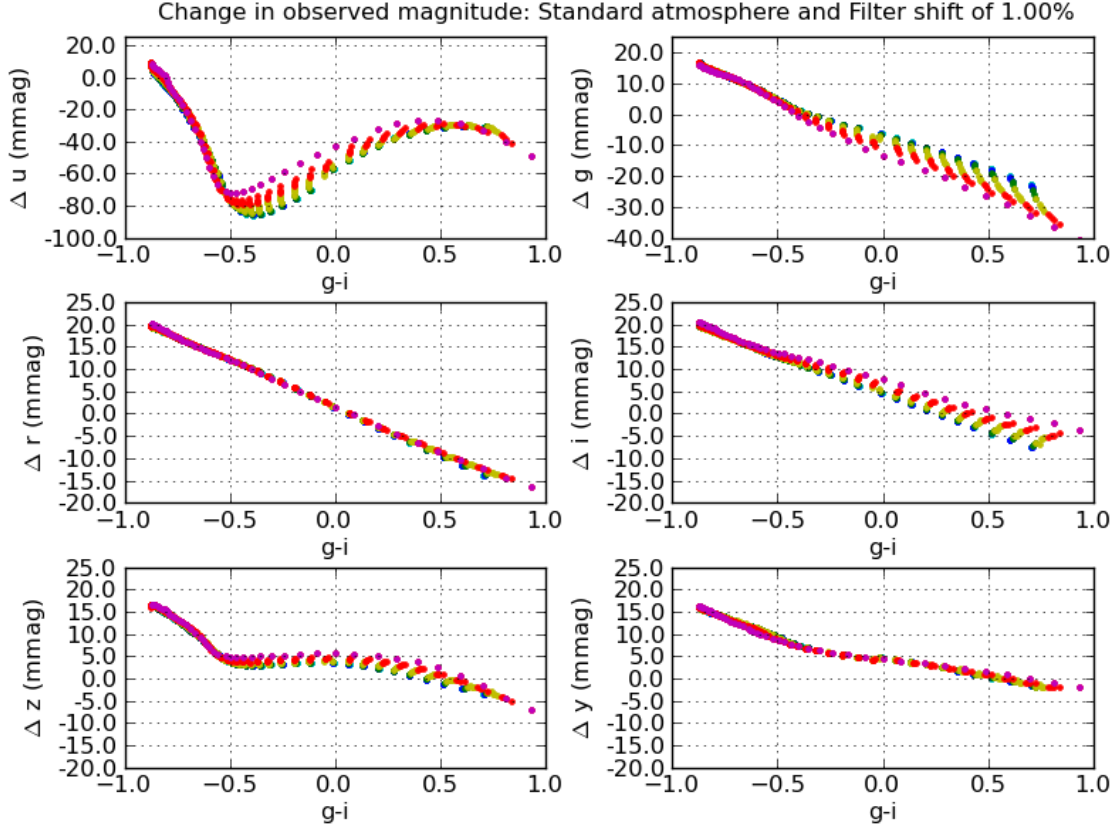
Figure 15: Δm_b^{obs} **due to a hardware response curve shift of 1% of the central wavelength of each bandpass.** 850 main sequence star Kurucz models with temperatures between 5000K and 35000K and metallicity indexes between -5.0 and 1.0 (solar) were combined with a standard atmosphere and standard hardware bandpass, and then with a total system response where the atmosphere remained constant but the hardware response was shifted by 1% of the central wavelength of each bandpass (as in Fig 12). The points in each plot are color-coded by metallicity, in steps of 1 dex between -5.0 (blue) to 1.0 (magenta). The resulting changes in observed natural magnitudes are on the order of 20 mmag typically, except in u band where the shift can create a δu of closer to 80 mmag for certain temperatures of main sequence stars. By measuring the bandpass shape as a function of radius and the colors of the main sequence stars, we can remove these effects.
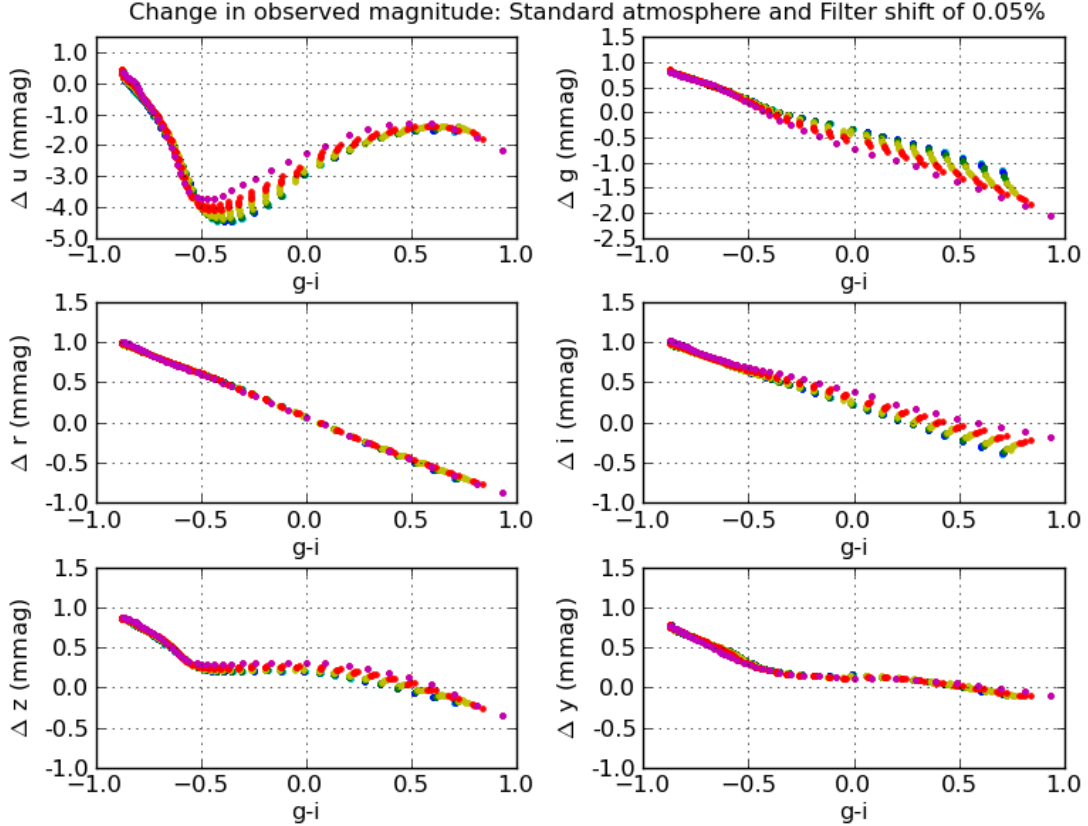
Figure 16: Δm_b^{obs} **due to a hardware response curve shift of 0.05% of the central wavelength of each bandpass.** Similar to Fig 13 except that the hardware response was shifted by only 0.05% of the central wavelength, an amount representing an unmeasured shift in the hardware response and thus contributing directly to the final error in the calibration of the natural magnitudes. Note that the y scale in these plots is reduced by a factor of 20 from Figure 13, consistent with measuring and compensating for the bandpass shift to within a 0.05% error.
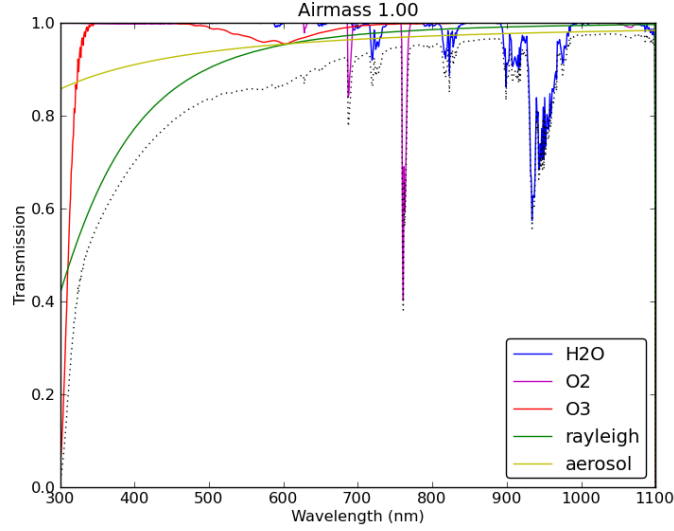
(a)
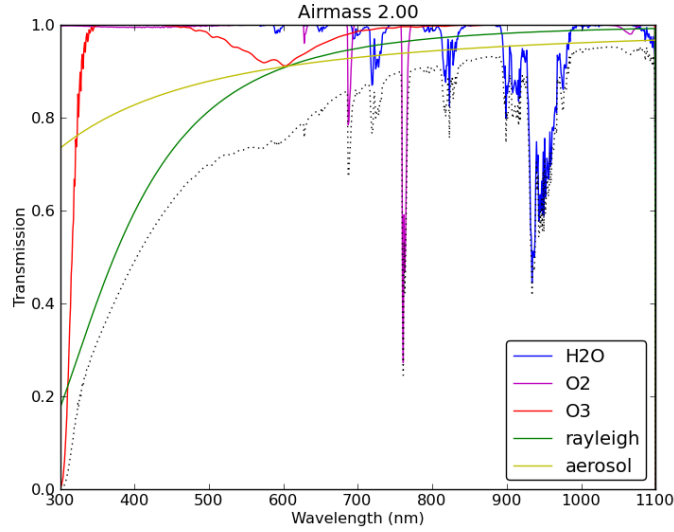
(b)

Figure 17: **Components of atmospheric absorption.** The wavelength dependence of various atmospheric absorption components at zenith (Panel 15a) and at airmass=2.0 (Panel 15b) are shown here. The H_2O (blue) and O_3 (red) molecular absorption contributions are shown separately, while the O_2 absorption is combined with other trace elements (magenta). A typical example of aerosol scattering (Mie scattering) is included (yellow), as is molecular scattering (Rayleigh scattering) (green). All components except aerosol scattering were generated using MODTRAN4 with the US Standard option (aerosol scattering is not part of the US Standard atmosphere). The resulting total absorption curve is the product of each of these effects and is shown with the dotted black line. This is an illustrative atmosphere; under actual observing conditions the molecular absorption components will vary in strength with time and the square root of the airmass, the molecular and aerosol scattering will depend on airmass, and the aerosol scattering profile will also vary with time.

5.2. Auxiliary Telescope

5.3. Water Vapor Monitoring System

5.4. Camera System Telemetry

6. Calibration Error Budget

7. Testing and Verification

The calibration process presented above is complex, and meeting the SRD requirements is dependent on understanding and controlling a large number of small perturbations. We seek to verify that our approach will produce the required results, and are doing so with different techniques that apply to the stages of LSST's construction and operation. During the current final design phase, we are employing simulation tools, backed up when possible by measurements on the sky from existing telescopes. (**?**) and (**?**) are examples of this approach. During the construction phase, we will be able to feed measured data from actual telescope components into the simulations. During operations, our focus is on designing metrics that will let us assess the calibration quality on an ongoing basis.

7.1. Repeatability

XXX-Testing our repeatability is rather trivial, as that does not require any external data. We simply apply the best-fit patch zeropoints to each patch and measure how well we make repeat measurements of each star.

7.2. Spatial Uniformity

XXX-We can compare to previous surveys. Pan-Starrs notes that they tend to see SDSS-shaped footprints in their residuals when comparing surveys. This will probably only put an upper limit on the uniformity, as LSST will be deeper and/or have larger coverage than available comparison surveys. Simulations can also help identify regions which we would expect could be poorly linked to the rest of the survey (this is expected to be a problem early in the survey before all regions of the sky have many well-linked observations). We can mesure very accurately our RMS as a function of patch and magnitude, and thus generate mock catalog realizations to run through the self-calibration procedure. These mock catalogs should give a good picture of the spatial uniformity.

7.3.   Flux Calibration

As mentioned in §4.2, there should soon be a system of white dwarf flux standards with HST observations. We can use subsets of these flux standards to make bootstrap estimates of our overall flux calibration. This is also a potential test of the spatial uniformity of the calibration, although this will be limited if the flux standards are concentrated on the equator.

7.4.   Color Calibration

There are now a number of techniques for comparing stellar colors accross the sky. **?** use a principle color analysis, **?** use a stellar locus regression, and **?** look at the color of main-sequence turn-off stars. For all of these techniques, the signal is usually dominated by dust extinction. However, at high galactic latitudes, the differences in stellar colors reveals errors in the calibration.

In addition to main-sequence stars, our flux standards should be useful for checking the color calibration. As with the flux calibration in a single band, we can exclude some of the flux standards from the analaysis and use the excluded stars to see how well we recover their colors.

8.   Software Implementation

TODO - new section on software implementation

Include : how do we calculate and apply color-correction terms, how do we use flat fields and illumination corrections, how/when do we run self-calibration and atmosphere fitting, and what do we report in DM (how do we store phi?)

8.1.   Level 2 Data Products

A. Filter Set

Figure 23 illustrates the baseline LSST filter bandpasses, including a 'standard' atmosphere, and baseline estimates for the mirrors, lenses, filter and detector transmission and sensitivity functions.

B. Areas for further investigation

LSST is pushing to improve traditional photometric accuracy by a factor of 2, through the use of independent measurements of the hardware and atmospheric transmission curve normalization and shape. As full-survey photometric calibration has never been attempted before at this level, there are understandably many areas which require further development and investigation. This section is intended to briefly document some of those areas.

- The broad-band flat field source spectrum. For simplicity, we have assumed above that the broad-band flat field is created using a white-light source SED. However, any source SED could be used to create the broad-band flat field, and an SED other than flat might be desireable. An SED which corresponds to the extincted spectrum of our fundamental standard might provide smaller systematic photometric errors when comparing individual stellar measurements to an absolute flux scale. On the other hand, an SED which matches an average calibration star could produce smaller systematic photometric errors in generating internally calibrated measurements. This choice of the source SED should be studied further.

- A cosmetic flat field. A photometric flat field, as discussed above, is necessary for photometric calibration. However, there may be some stages of image processing where a 'cosmetic' flat field, which creates a flat background sky is desirable (instead of the photometric flat field, which creates a background sky which varies according to the geometric size of the pixels). The details of the production of the photometric flat field, the image processing, and whether a cosmetic flat field is necessary must be discussed among the various software teams working on LSST.

- The illumination correction. As discussed in the document above, the photometric uniformity which must be achieved from the broad-band flats is a significant source of error in the final photometric calibration. Some of this photometric uniformity is currently achieved through extremely strong constraints on the dome screen illumination pattern, while some will be achieved through a combination of forward modeling of the optical path (a ZEMAX model) and rastering dense fields of bright stars across the

focal plane. We strongly suspect that the self-calibration procedure can compensate for a much greater non-uniformity in the photometric flat than is currently budgeted; that is, the self-calibration procedure can help build a more accurate illumination correction to apply to the observed flat field. The exact limits of the self-calibration procedure in building an illumination correction in the face of realistic errors from the bandpass shape correction and atmospheric extinction must be explored in more detail.

- Hardware response curve - $\phi_b^{sys}(\lambda, t)$. There is a narrow-band dome screen projector system installed at Pan-STARRS which will be extremely useful to study for comparison to the planned LSST dome screen. The Pan-STARRS system has demonstrated that ghosting is a significant problem in the narrow-band flat field, and must be compensated for in a narrow-band illumination correction (one per narrow-band flat, as this ghosting is wavelength dependent). Some methods for measuring the ghosts in the Pan-STARRS system as a function of wavelength have already been implemented (Chris Stubbs, private communication), and these tests will feed back to the plans for the LSST dome screen projectors. LSST must continue to improve our ZEMAX modeling of these updated projector screens with expected LSST optical components to study ghosting, as well as how the error induced by these wavelength-dependent ghosts propagates through the rest of calibration. In addition, we will investigate how the self-calibration procedure could contribute towards compensating for these narrow band, wavelength-dependent illumination corrections. A major problem in attempting to generate narrow-band illumination corrections from the self-calibration procedure is that these illumination corrections would then only be appropriate for main-sequence SEDs (as these are the stars used in self-calibration); we must investigate how these could be applied to non-main-sequence SEDs.

- Atmospheric absorption - $\phi_b^{atm}(\lambda, t)$. Further observing runs where spectroscopic (and preferably, also broad-band photometry) observations of known sources under a wider variety of weather conditions and at a variety of pointings over the sky will be obtained to verify that the range of atmospheric conditions described in Section ?? are appropriate and that the model used to describe the water vapor variation across the sky is adequate. This is particularly important when considering y band photometric calibration and will feed back into the observation plan for the auxiliary telescope. Using data acquired in these observing runs, we will also test the wavelength resolution necessary for the auxiliary telescope.

- Cloud extinction. The expected cloud structure function at Cerro Pachón is not well understood; the extent of its 'clumpiness' as a function of total cloud extinction is a significant unknown in the self-calibration procedure. LSST plans to install small

wide-field camera systems to measure cloud extinction across the sky and on small scales on Cerro Pachon to address this issue.

- Self-calibration. The self-calibration software must be developed further to run efficiently on full LSST data sets. Work is already underway to test alternative solver methods (conjugate gradient, least-squares) and add multi-threading to the solver, to both speed up the self-calibration procedure and to to handle more observations of more stars, requiring more memory. The extent to which additional terms can be added to the model magnitude with each of these algorithms will also be investigated. In addition, further tests to probe the boundaries of 'where self-calibration breaks down' will be conducted for each parameter and updated as the algorithms are improved. The self-calibration algorithm will also be included into LSST Data Challenges and applied to real-world data, as well as data from the LSST end-to-end simulations.

- Effects on non-main sequence stars. Each of the calibration steps above have been considered in terms of main sequence stars (as these become the 'calibration' stars for self-calibration). The wavelength-independent stages are identical for main-sequence or non-main-sequence stars. However, the wavelength-dependent corrections have differing effects on non-main sequence or extreme SEDs. For example, the results of a 30% H_2O variation may have a much larger effect on the final calibrated magnitudes for MLT dwarfs (which have many absorption and emission lines in and near the y band) than the same 30% variation did on the main sequence stars. Section C describes these effects further. Further modeling is required to understand the full photometric calibration potential for all types of objects that LSST will observe, with consideration of the potential photometric calibration accuracy for objects for which the SED may not be well known (such as SN with an unknown redshift).

- External calibration standards, for both band-to-band and absolute calibration. These calibration standards need to be identified and observing programs to determine full spectro-photometric characteristics for the required sample must be conducted. The required size of this sample is approximately known, but should be studied further.

C. Photometric measurements for non-main sequence stars

LSST will record a series of m_b^{nat} measurements for each astronomical object in each visit. These m_b^{nat} measurements are generated directly from the counts recorded in each image, corrected with the photometrically uniform, broad-band flat field and for gray (cloud) atmospheric extinction effects. However, these m_b^{nat} measurements will vary as the shape of

the bandpass changes, whether as a function of position in the focal plane or as a function of changes in atmospheric absorption components. Correcting for these effects requires assuming a particular SED for each source, and produces m_b^{std} values after applying Δm_b^{meas} offsets (see the overview of calibration in section 3.2 for a review).

For most objects, LSST will simply assume the source has a flat SED, which means that m_b^{std} is exactly equal to m_b^{nat}, as by definition then Δm_b^{meas} is zero. To permit scientists to generate higher precision photometry for objects using arbitrary SEDs, LSST must provide a record of $\phi_b^{meas}(\lambda, alt, az, x, y, t)$ as well as the normalization zeropoint offsets for each observation. With these additional pieces of information, scientists can generate more appropriate Δm_b^{meas} corrections, using their own chosen object SED to generate m_b^{std}. Sections ?? and ?? outline the typical magnitudes of these corrections for main sequence stars; Δm_b^{meas} can easily be on the order of 20 mmag for gri, or even 100 mmag in u band. For more extreme SEDs, these corrections may be even larger.

Figure 24 illustrates the likely magnitude of these Δm_b^{meas} corrections for a wide variety of SEDs. In each plot, the main sequence stars are shown as in the figures in the main paper (small dots, color-coded by metallicity), although given the increased scale here they only appear as a purple series of circles. M dwarfs are now included, generally mimicking the behavior of the main sequence stars but extending further into the red. More unusual SEDs are also included; a quasar SED, based on a composite of many empirical quasars from SDSS from ? that has been extended to the full LSST wavelength range through the addition of power law flux above and below the original range ($f_\nu \propto 1/\lambda^{0.5}$ for $\lambda < 89$nm & $f_\nu \propto 1/\lambda^{1.5}$ for $\lambda > 800$nm), and redshifted from $z = 0$ to $z = 3$; also a sample of SN Ia from templates generated by Peter Nugent (?), redshifted from $z = 0$ to $z = 1$.

The figure shows the Δm_b^{meas} values that would be expected under a maximum change of atmospheric parameters and under a likely bandpass shift. This demonstrates how much the reported m_b^{nat} values could vary for each object. If LSST was to just calculate an offset between m_b^{nat} and m_b^{std} based on an object's color (and assuming that the object had an SED similar to a main sequence star), the resulting m_b^{std} values would be incorrect by the value of the offset between the true Δm_b^{meas} for the SED and the main sequence Δm_b^{meas} values at each color; this could easily be more than 20mmag.

With the wide variety of objects and SEDs that will be possible in the LSST data set, it is crucial to provide the information and tools so that scientists may calculate highly precise m_b^{std} magnitudes for their objects of interest. This means recording or providing the means to recalculate $\phi_b^{sys+atm}(\lambda, t)$ for every object detected with LSST.

D.   Glossary

- **Level 1 Data Product.** A data product, such as a measurement of an astronomical object's position or flux in a single image, that is computed on a nightly basis. Level 1 data products primarily consist of alerts on transient, variable and moving objects. The photometric calibration process outlined in this paper does not apply to Level 1 data products. Level 1 data products will be calibrated using all applicable prior knowledge (including secondary standard catalogs generated from previous Data Release calibration of all LSST-observed stars in the field).

- **Level 2 Data Product.** A data product, such a measurement of an astronomical object's position or flux in either a single image or a series of images, that is computed on the Data Release schedule, on a six-month or yearly schedule. Level 2 data products leverage all previous observations of the same object, as well as all knowledge of the LSST system accumulated to that point. The photometric calibration process outlined in this paper is used to generate Level 2 data products.

- **Normalized system response, $\phi_b(\lambda)$.** The normalized system response describes the shape of the bandpass transmission curve, separating this from the normalization of the throughput curve which can be determined separately. $\phi_b(\lambda)$ is described by Equation 5. The integral of $\phi_b(\lambda)$ is always 1.

- **Camera Calibration Optical Bench (CCOB)**. The CCOB is an apparatus to calibrate the spatial and wavelength-dependent response of the focal plane (detector + camera). The CCOB uses a well controlled, wavelength-variable, light source (such as a tuneable laser) calibrated using a NIST photodiode to illuminate the focal plane when the camera is unmounted from the telescope. This light source, which produces a spot in the focal plane approximately the size of or smaller than the PSF, will be scanned across the detector (x, y) at a variety of beam incident angles, (θ, ϕ) and at a variety of wavelengths (λ). This allows the response of the detector to be measured in the presence of a well-understood light source. The response of the detector can be measured in two different configurations: one with only the detector and the dewar window - which doubles as lens 3 (L3) - and one with the detector, L3, L2, L1, a small test-section of filter and the camera shutter. The filter test section used is not the full LSST filter, and thus will not capture spatial non-uniformities in the filter bandpass. The CCOB provides test data about the camera assembly for camera acceptance and will help constrain the optical ZEMAX model, although without a full filter it cannot capture the full set of parameter required for the ZEMAX model. More details about the requirements and physical apparatus of the CCOB are available in LSST-10015

and LSST-8217.

- **Broadband flat field.** An image obtained by observing a light source which generates photons with a wide range of wavelengths (as opposed to a narrow-band flat), with relatively uniform illumination across the field of view. Night sky flats, twilight flats, and white-light or broadband dome screen flats would all generate broadband flat fields.

- **Narrow-band flat field.** An image obtained by observing a light source which generates photons with a very narrow range of wavelengths (hypothetically, even a single wavelength), with relatively uniform illumination across the field of view. A dome screen illuminated with a narrow-band laser light source will generate a narrow-band flat field.

- **'Observed' flat field.** A flat field, as obtained by observing the dome screen projectors. Generally would refer to a broadband flat field.

- **Photometric flat field.** A flat field which produces uniform photometric measurements across the field of view for a flat $F_\nu(\lambda)$ source. A photometric flat field must be based on a broadband flat.

- **Illumination Correction.** The ratio between the photometric flat field and the observed flat field.

$$\mathrm{Flat_{photometric} = Flat_{observed} * IlluminationCorrection} \qquad \mathrm{(D1)}$$

.

- **Natural magnitude.** A magnitude measurement which relates directly to the number of counts measurement in an image (after including a photometric flat field correction and a rough zeropoint for an entire image). The natural magnitude relate to an ADU count that does *not* account for the color or SED of the source being observed, thus does not include any wavelength-dependent corrections. For a non-variable source observed under variable atmospheric transmission conditions and/or at varying locations in the field of view, the natural magnitude reported will change due to changes in the bandpass shape. The natural magnitude is equivalent to an observed magnitude, after the appropriate zeropoints have been applied.

- **Standard magnitude.** A magnitude measurement which includes not only corrections for the photometric flat field and a rough zeropoint for the image, but also includes a correction for wavelength-dependent effects. This means the Δm_b^{meas} appropriate to correct the natural magnitude of the object from the observed bandpass

shape, $\phi_b^{meas}(\lambda, t)$, to the standard bandpass shape, $\phi_b^{std}(\lambda)$, has been calculated for the SED of the object and applied. For a non-variable source, m_b^{std} will be constant over time even if the atmospheric absorption curve or the location in the field of view changes.

- **Operations Simulation.** The Operations Simulation is a simulated pointing history of LSST, covering the sky in the same manner as the telescope could, in practice. It uses weather conditions based on historical records from Cerro Tololo, including appropriate seeing and sky brightness variations. The motion of the telescope is simulated in high fidelity, including acceleration from field to field and cable wrap. A variety of proposals are used to determine which fields to observe at each time; these proposal include the 'universal cadence' (satisfying most of LSST's science requirements) and 'deep drilling' (a limited set of fields, observed frequently and deeply over the lifetime of the survey).

- **PWV.** Precipitable Water Vapor. The total column depth of water vapor in the atmosphere, measured at zenith. The units are mm of liquid water equivalent.
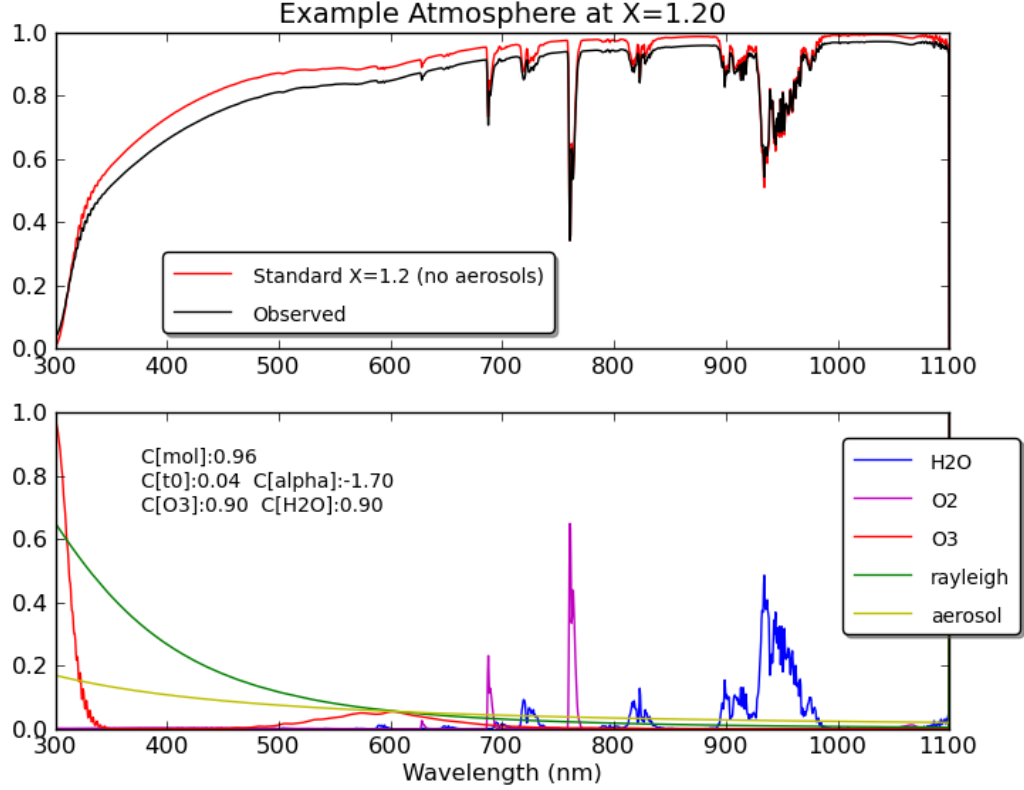
Figure 18: **Example of an atmosphere generated from a typical mix of atmospheric components.** The bottom panel shows the MODTRAN absorption templates at this airmass used in generating the final atmosphere (the $A_{rayleigh/O_2/O_3/H_2O}$ and $A_{aerosol} = 1 - e^{\tau_{aerosol}}$ from Equation **??**). The top panel shows the final combined atmospheric transmission curve in black, as well as a 'standardized' atmospheric transmission curve in red. This demonstrates that (even without using the full MODTRAN software, just the transmission templates) that we can closely recreate any atmosphere desired with any composition.

(a)

(b)

(c)

(d)
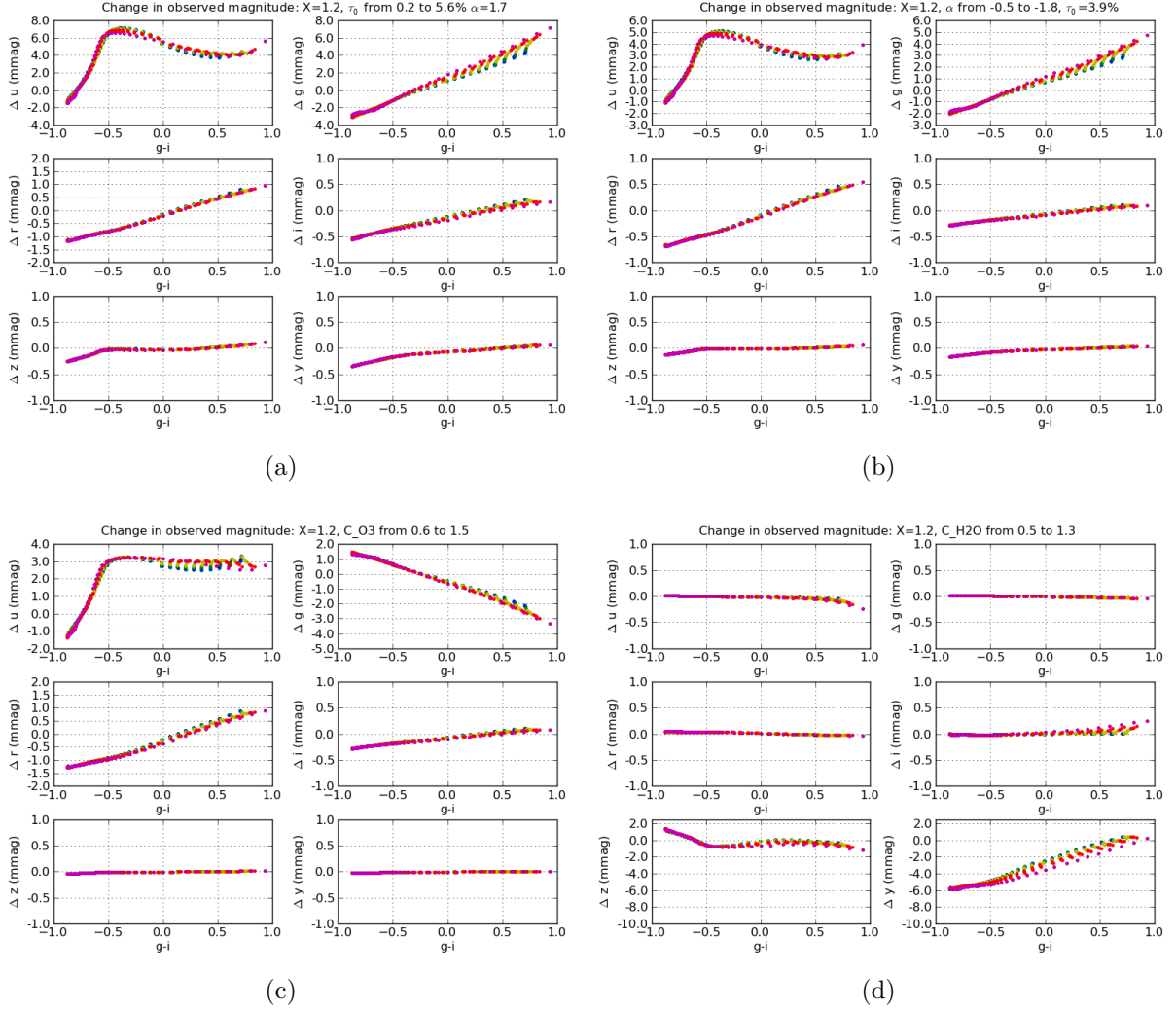
Figure 19: Δm_b^{obs} **due to variations of each individual absorption component.** Each atmospheric transmission curve (at X=1.2) was combined with the set of main sequence Kurucz curves to determine the resulting changes in observed magnitudes, as in Figure 13. Panels 17a and 17b show the effects of varying aerosol absorption in τ_0 and α respectively, Panel 17c shows the effect of varying O_3 absorption. These effects are concentrated in u and g bands, with a negligible effect in izy. Panel 17d shows the effect of varying the H_2O absorption, which is strongest in y, with some effect in z and no effect in $ugri$.
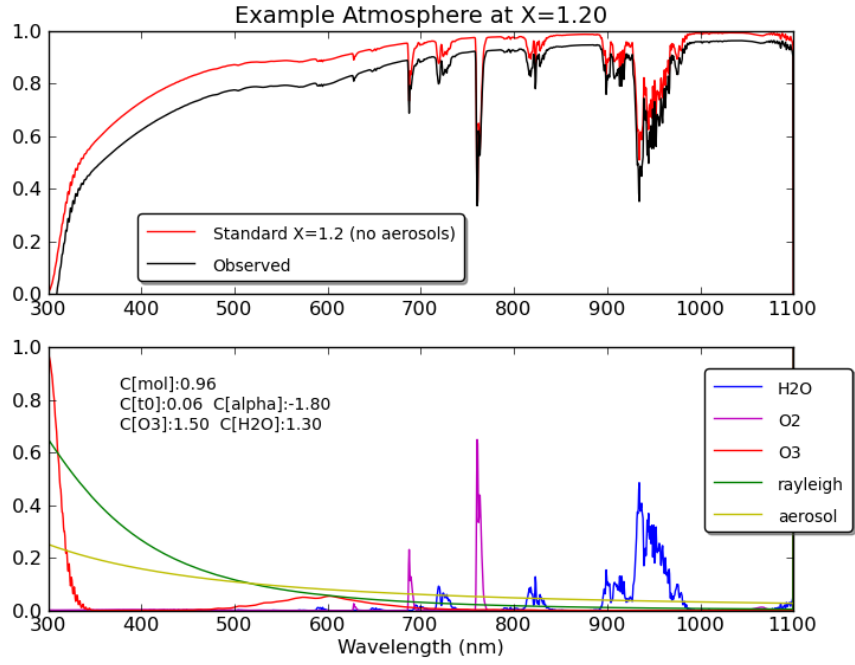
(a)
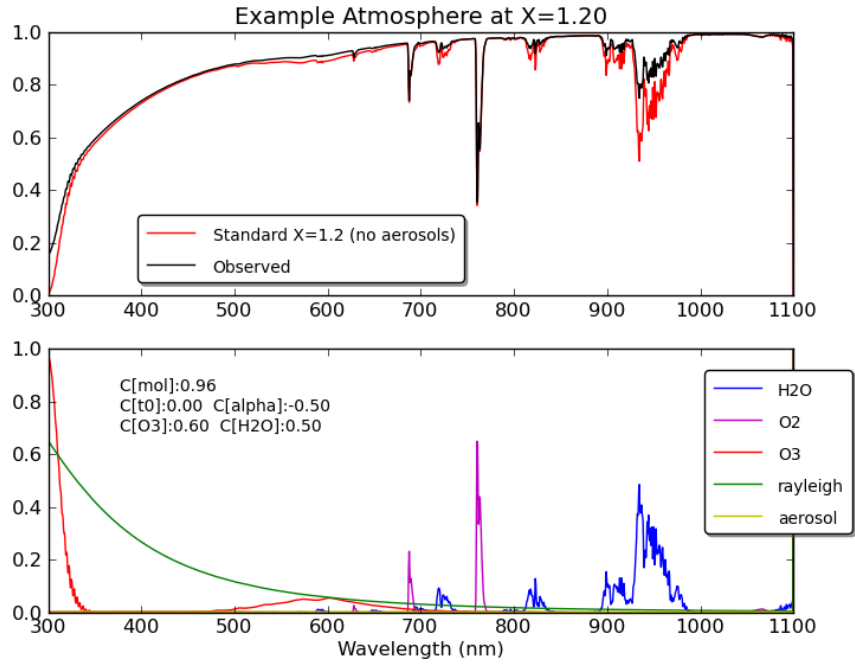
(b)

Figure 20: **'Extreme' atmospheres generated from MODTRAN profiles and extremes of atmospheric coefficients.** Using the extremes of C_{H_2O}, C_{O_3}, and τ_0 and α from **?**, two test atmospheres with $X = 1.2$ were created using Equation **??**.
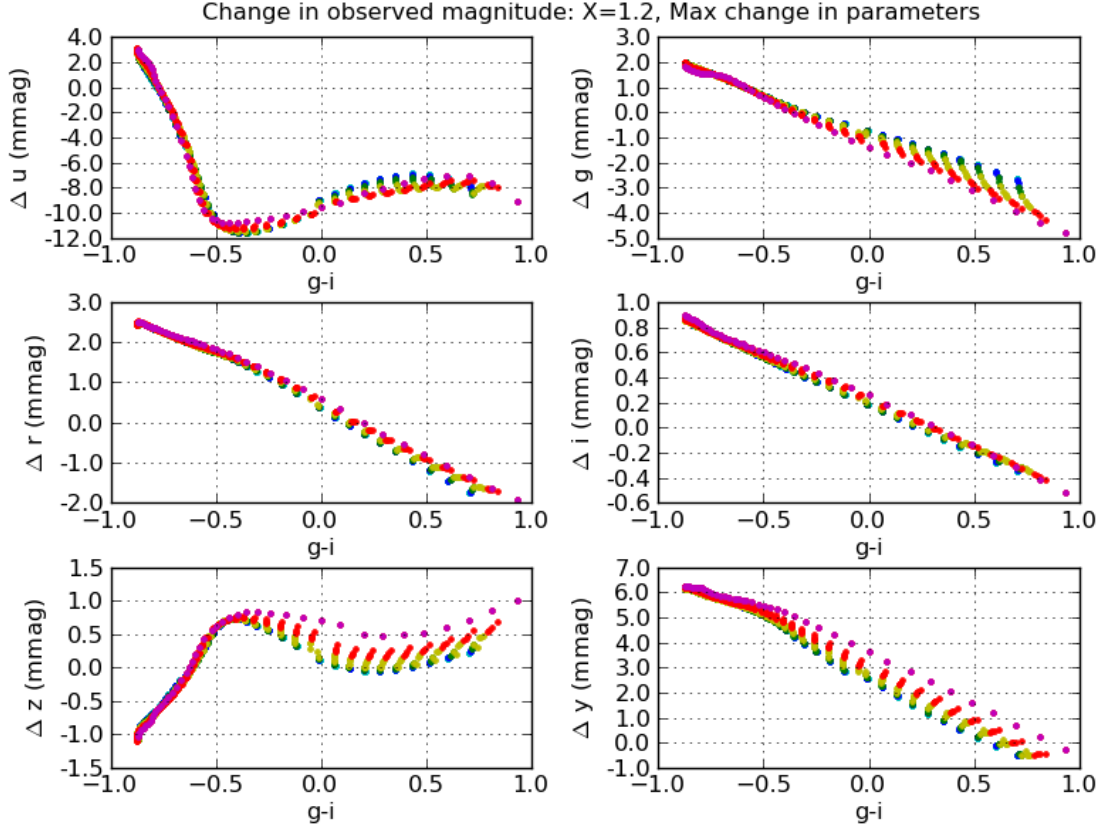
Figure 21: Δm_b^{obs} **due to 'extreme' variations of atmospheric transmission.** Two atmospheric transmission curves were created using Equation **??** and the widest variations of atmospheric extinction coefficients from **?**. The wavelength profile of these atmospheres is shown in Figure 18. These atmospheric transmission curves were combined with the baseline LSST hardware transmission curves, and used to generate magnitudes for 850 Kurucz models with temperatures between 5000 K and 35000 K and metallicities between -5.0 and 1.0 (solar). The resulting differences in natural magnitudes between the two extremes of the atmospheric transmission in each filter are shown above.
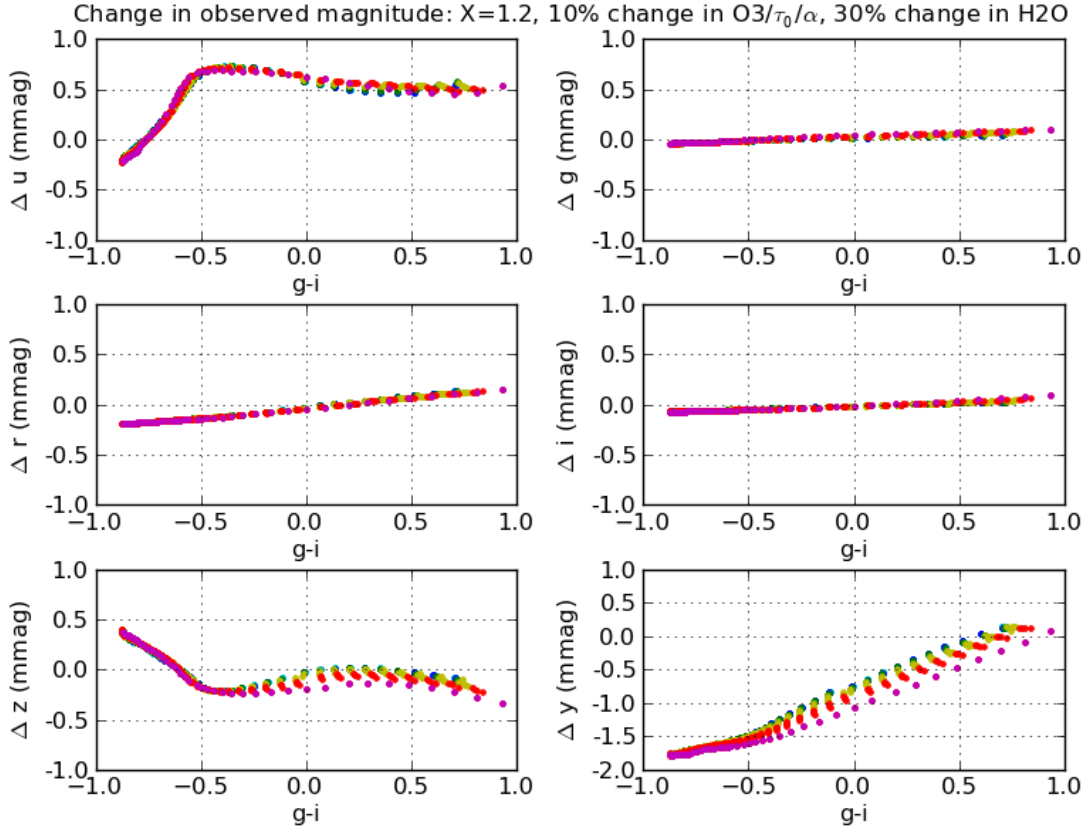
Figure 22: Δm_b^{obs} **due to 10% variations of atmospheric transmission in O$_3$ and aerosol, with 30% variation of H$_2$O.** This is similar to Figure 19, except C_{O_3}, τ_0 and α were only varied by 10% of the total range of values measured in **?**, and C_{H_2O} was varied by 30% of the total range.
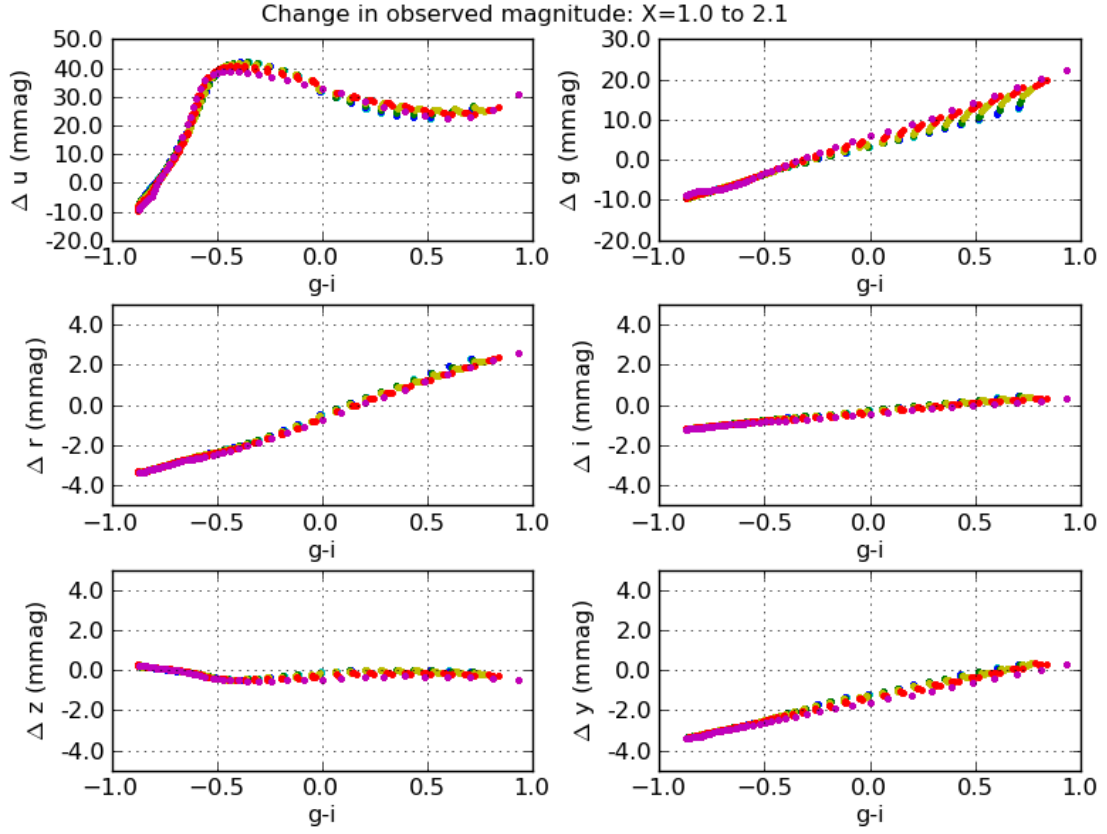
Figure 23: Δm_b^{obs} due to changes in airmass from $X = 1.0$ to $X = 2.1$, for a typical atmospheric transmission response curve.
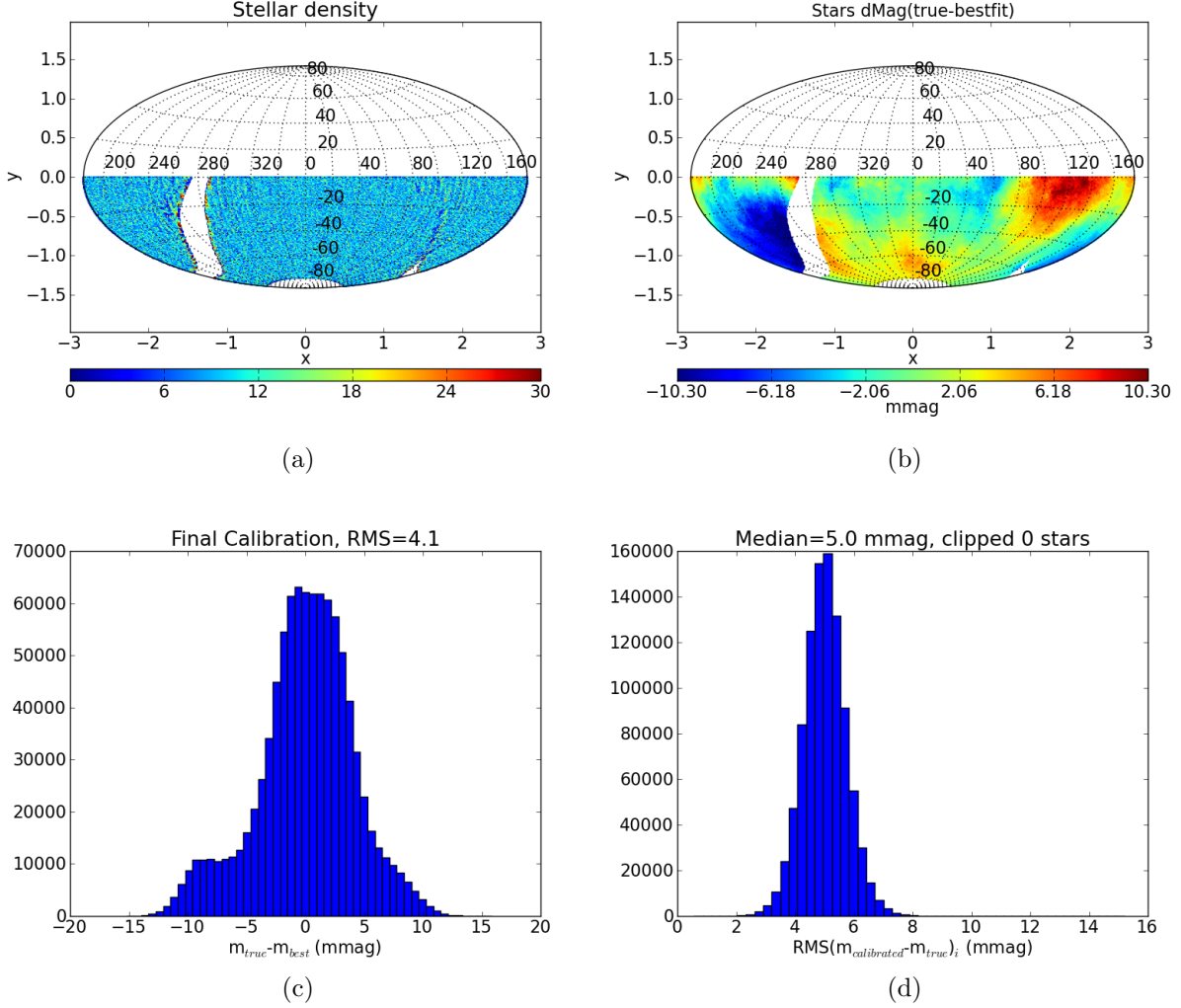
(a)

(b)

(c)

(d)

Figure 24: **Results from a self-calibration investigation.** Panel 22a shows the stellar density across the sky relevant for the simulation - note the Milky Way plane has been cut out of the simulation, and we have only used pointings with declination between -80 and 0 degrees. Conditions for this simulation are described in the text. Panel 22b shows the true minus best-fit stellar magnitudes residuals across the sky after iterating the self-calibration solver. Panel 22c shows similar information, but as a histogram of all stars, demonstrating the 'uniformity' requirement in the SRD. Panel 22d shows a histogram of the RMS of the difference between the calibrated and true magnitudes for each star (after self-calibration iteration), demonstrating the 'repeatability' requirement in the SRD.
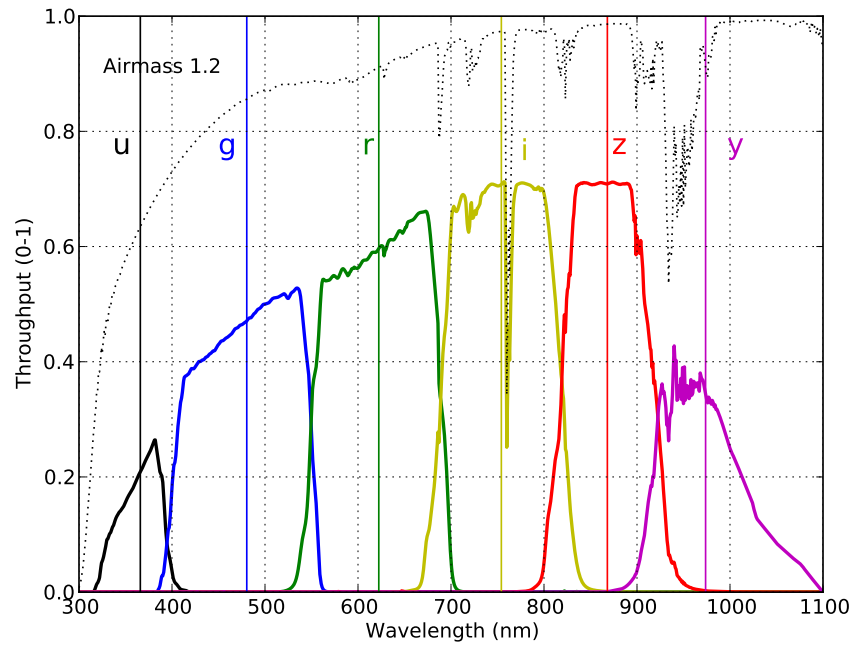
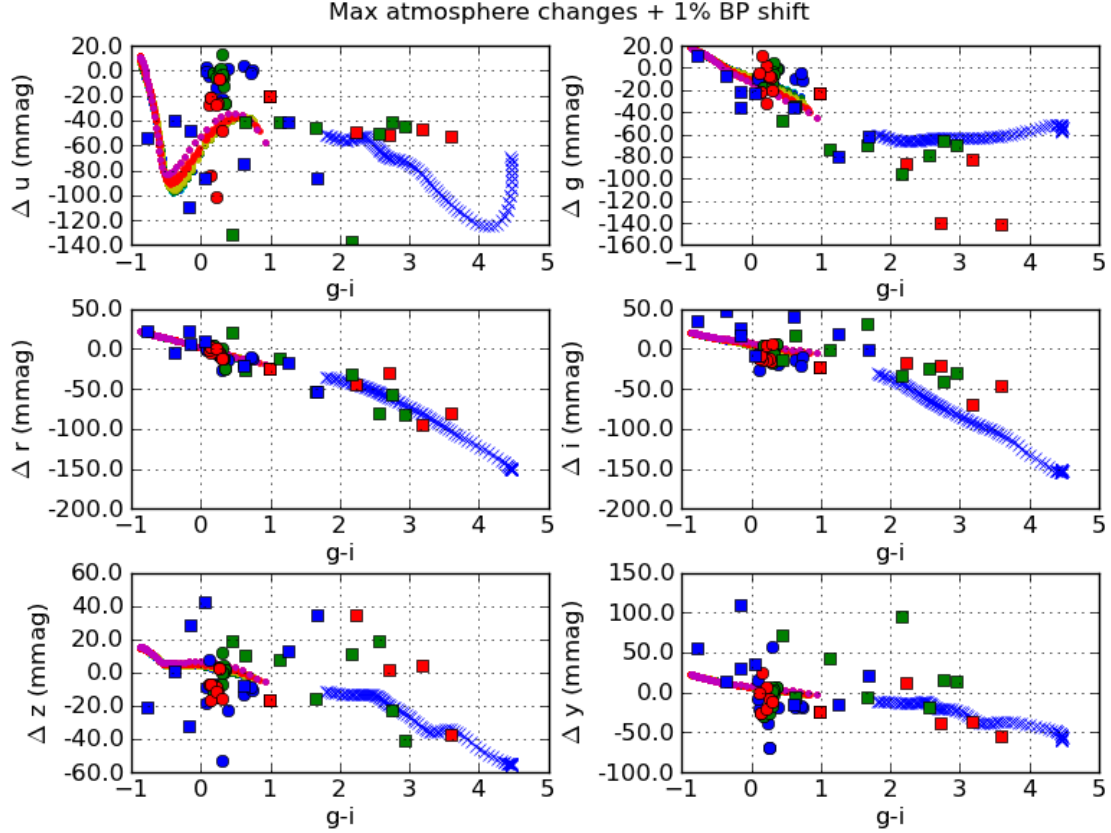Figure 25: **The baseline LSST filter set.**

Figure 26: Δm_b^{obs} **due to changes in a hardware bandpass shift and a maximum change in atmospheric absorption components.** This plot is similar in nature to a combination of Figure 13 and 19, but has been extended to include a wider variety of object SEDs. Main sequence stars are shown as the sequence of purple dots, and Mdwarfs are shown as the sequence of blue 'x's. The large round circles represent a quasar SED at various redshifts, color-coded with redshift as follows: $0 < z < 1$ is blue, $1 < z < 2$ is green, and $2 < z < 3$ is red. The large filled squares show the change in natural magnitudes for SNIa templates at times of 0, 20, and 40 days from peak; $0 < z < 0.36$ are blue squares, $0.36 < z < 0.72$ are green squares, and $0.72 < z < 1$ SNIa are red squares.